A Computational Framework For Generating Rotation Invariant Features And Its Application In Diffusion MRI

Mauro Zucchelli, Samuel Deslauriers-Gauthier, Rachid Deriche

A Computational Framework For Generating Rotation Invariant Features And Its Application In Diffusion MRI

Mauro Zucchelli[a], Samuel Deslauriers-Gauthier[a], Rachid Deriche[a]

[a] *Athena Project-Team, Inria Sophia Antipolis - Méditerranée, Université Côte D'Azur, France*

Abstract

In this work, we present a novel computational framework for analytically generating a complete set of algebraically independent Rotation Invariant Features (RIF) given the Laplace-series expansion of a spherical function. Our computational framework provides a closed-form solution for these new invariants, which are the natural expansion of the well known spherical mean, power-spectrum and bispectrum invariants. We highlight the maximal number of algebraically independent invariants which can be obtained from a truncated Spherical Harmonic (SH) representation of a spherical function and show that most of these new invariants can be linked to statistical and geometrical measures of spherical functions, such as the mean, the variance and the volume of the spherical signal. Moreover, we demonstrate their application to dMRI signal modeling including the Apparent Diffusion Coefficient (ADC), the diffusion signal and the fiber Orientation Distribution Function (fODF). In addition, using both synthetic and real data, we test the ability of our invariants to estimate brain tissue microstructure in healthy subjects and show that our framework provides more flexibility and open up new opportunities for innovative development in the domain of microstructure recovery from diffusion MRI.

Keywords:

Diffusion MRI, Rotation Invariants, Spherical Harmonics, Gaunt Coefficients, biomarkers

1. Introduction

Diffusion Magnetic Resonance Imaging (dMRI) signals are influenced by several parameters such as the diffusion gradient strength, the pulse width, the diffusion time, and the direction of the gradient. Each of these parameters can be tuned and changed to be sensitive to a particular characteristic of the biological tissue under examination. In brain imaging, for example, the variation of gradient strength and diffusion time have been exploited to measure tissue microstructural features such as axonal diameter (Assaf et al., 2008), water diffusivity (Kaden et al., 2016a,b; Novikov et al., 2018a), and neurite density (Zhang et al., 2012; Jespersen et al., 2007, 2010). Changes in the gradient direction have made it possible to measure the average anisotropy of the tissues (Frank, 2002), the profile of the water molecules displacement (Özarslan et al., 2013) and the white matter fiber orientation distribution (Tournier et al., 2004).

In many applications this directional dependence is desirable (e.g. tractography), while in others, it is a hindrance because it introduces signal changes which are independent of the quantity that we want to estimate (e.g. neurite density estimation). Several techniques have been developed to remove the directional dependency of the diffusion signal and improve microstructural indexes estimation such as the powder-averaging (Edén, 2003; McKinnon et al., 2017) which is also known as Spherical Mean Technique (Anderson, 2005; Kaden et al., 2016a), the Bayesian approach proposed by Reisert et al. (2016), and the Linearly Estimated Moments provide Orientations of Neurites And their Diffusivities Exactly (LEMONADE) (Novikov et al., 2018a). All these techniques take advantage of a rotationally invariant representation of the diffusion signal to factor out its directional dependency. The search for rotation invariant descriptors of spherical functions is an independent field of research that interests not only dMRI (Caruyer and Verma, 2015) but also computer vision (Kondor, 2007) and pattern recognition (Kakarala and Mao, 2010). Two of the most widely used dMRI rotation invariant features (RIF) are Mean Diffusivity (MD) and Fractional Anisotropy (FA) (Basser et al., 1994) which can be calculated

from a rank-2 tensor representation of the Apparent Diffusion Coefficient (ADC) profile (Özarslan and Mareci, 2003).

In general, the construction of an RIF starts with the Laplace-series expansion of the considered spherical function. Thanks to this representation, the signal can be approximated by a truncated sum of Spherical Harmonics (SH) weighted by the series coefficients. The number of coefficients, n_c, depends on the degree[1] L, at which the series is truncated. The number of *algebraically independent* RIF that can be obtained from a truncated SH series is equal to the number of SH coefficients minus three, the degree of freedom of the rotation operator (Ghosh et al., 2012a; Caruyer and Verma, 2015). Algebraic independence is a fundamental property that ensures that none of the elements of the considered set of RIF can be expressed as an algebraic function of one or more of the other elements of the set. This characteristic enables us to obtain a non-redundant representation of the rotation invariant properties of a spherical function.

In this work, we propose a new framework for analytically generating a complete set of algebraically independent RIF given the Laplace-series expansion of a spherical function. The resulting invariant set unifies the results of previously proposed invariants framework such as the power-spectrum (Novikov et al., 2018a) and the bispectrum invariants (Kondor, 2007) under the same mathematical umbrella. In addition, our framework extends these invariants sets in order to reach a complete set of algebraically independent RIF. Part of this work has been presented in Zucchelli et al. (2018b). In this new extended version we were able to: i) provide a more solid mathematical background linking the new invariants to physical quantities with a clear numerical definition such as the variance and the volume of the spherical signal (Section 2); ii) present two new applications of our RIF to dMRI signal modeling both the ADC profile and the diffusion signal itself (Section 3). In Section 4 we will present the data set

[1]In this work we use the word *degree* for the SH frequency index l, the word *order* for the SH phase index m, and the symbol L for the truncation degree.

used in this work and in Section 5 we will show that our invariants can aid in the calculation of microstructural features[2] in both, the ADC and the diffusion signal. Finally, in Section 6 we will discuss our results and in Section 7 we will draw conclusions from our work.

2. Theory

Consider a real valued spherical function $f(\mathbf{u})$ parameterized by the 3D unit vector $\mathbf{u}$. Its Laplace-series expansion can be calculated as

$$f(\mathbf{u}) = \sum_{l=0}^{\infty} \sum_{m=-l}^{l} c_{lm} Y_l^m(\mathbf{u}) \tag{1}$$

where Y_l^m are the real SH (Descoteaux et al., 2007; Homeier and Steinborn, 1996) of degree l and order m (see Supplementary Material Section 1 for the definition of real SH and their properties). The SH coefficients c_{lm} can be analytically calculated as

$$c_{lm} = \int_{S^2} f(\mathbf{u}) Y_l^m(\mathbf{u}) d\mathbf{u} \tag{2}$$

with $S^2 = \{\mathbf{u} \in \mathbb{R}^3 : \|\mathbf{u}\| = 1\}$. The application of a rotation operator $\mathbf{R}$ to a SH can be written as

$$\mathbf{R} Y_l^m(\mathbf{u}) = Y_l^m(\mathbf{R}^{-1}\mathbf{u}) = \sum_{m'=-l}^{l} D^l_{m',m}(\mathbf{R}) Y_l^{m'}(\mathbf{u}) \tag{3}$$

with

$$D^l_{m',m}(\mathbf{R}) = e^{-im'\alpha} d^l_{m',m}(\beta) e^{-im\gamma} \tag{4}$$

where α, β, and γ are the Euler angles and $d^l_{m',m}$ represents the *Wigner d function* (Baxansky and Kiryati, 2007). We can define $h(\mathbf{u}) = \mathbf{R} f(\mathbf{u})$ as the

[2]Following the works of Novikov et al. (2018a) and Lampinen et al. (2017) we consider the apparent intra-axonal signal fraction, the parallel diffusivity, and the extra-axonal perpendicular diffusivity as microstructural features.

rotation of the function f whose SH expansion is given by

$$\begin{aligned} h(\mathbf{u}) = \mathbf{R}f(\mathbf{u}) &= \sum_{l=0}^{\infty} \sum_{m=-l}^{l} c_{lm} Y_l^m(\mathbf{R}^{-1}\mathbf{u}) \\ &= \sum_{l=0}^{\infty} \sum_{m'=-l}^{l} g_{lm'} Y_l^{m'}(\mathbf{u}) \end{aligned} \tag{5}$$

and rotated SH coefficients $g_{lm'}$ are given by

$$g_{lm'} = \sum_{m=-l}^{l} c_{lm} D^l_{m',m}(\mathbf{R}). \tag{6}$$

A generic RIF, denoted by I, of a spherical function f can be expressed as a functional for which

$$I[f(\mathbf{u})] = I[\mathbf{R}f(\mathbf{u})], \ \forall \mathbf{R}. \tag{7}$$

In the following subsections, we will investigate several known statistical and geometrical RIF such as the mean, the variance, and the volume of a spherical function. By identifying the common pattern between these physical invariants and their relation to well-known invariants such as the *power-spectrum* and *bispectrum* invariants (Kondor, 2007) we will derive a generic framework for analytically generating rotation invariants for the truncated SH representation of a spherical function.

2.1. Mean of the signal and Spherical Mean invariant

Intuitively, the mean of a spherical function is a rotation invariant feature. In fact, the mean of $f(\mathbf{u})$ can be calculated as

$$\begin{aligned} I_{mean}[f] &= \frac{1}{4\pi} \int_{S^2} f(\mathbf{u}) d\mathbf{u} \\ &= \frac{1}{4\pi} \int_{S^2} \sum_{l=0}^{\infty} \sum_{m=-l}^{l} c_{lm} Y_l^m(\mathbf{u}) d\mathbf{u} \\ &= \frac{1}{4\pi} \sum_{l=0}^{\infty} \sum_{m=-l}^{l} c_{lm} \int_{S^2} Y_l^m(\mathbf{u}) d\mathbf{u} \\ &= \frac{1}{4\pi} \sum_{l=0}^{\infty} \sum_{m=-l}^{l} c_{lm} \sqrt{4\pi} \delta_{lm}^{00} \\ &= \frac{1}{\sqrt{4\pi}} c_{00} \end{aligned} \tag{8}$$

Indeed, $I_{mean}[f]$ represents an RIF:

$$I_{mean}[f] = \frac{1}{4\pi}\int_{S^2} f(\mathbf{u})d\mathbf{u} = \frac{1}{4\pi}\int_{S^2} f(\mathbf{R}^{-1}\mathbf{u})d\mathbf{u}. \tag{9}$$

This equivalence follows from the fact that the area underneath a function is invariant to rotation. This invariant, also known as SMT (Spherical Mean Technique), was the first RIF used in dMRI to obtain a rotation invariant microstructural index estimation by Kaden et al. (2016a).

2.2. Variance of the signal and power-spectrum invariants

The mean is the first-order moment of a function. The second central order moment – the variance – is also rotation invariant. The variance of the signal can be calculated by

$$I_{variance}[f] = \frac{1}{4\pi}\int_{S^2} \left(f(\mathbf{u}) - I_{mean}[f]\right)^2 d\mathbf{u}. \tag{10}$$

Considering the SH expansion of $f(\mathbf{u})$ this is equal to

$$\begin{aligned}
I_{variance}[f] &= \frac{1}{4\pi}\int_{S^2}\left|\sum_{l=0}^{\infty}\sum_{m=-l}^{l} c_{lm}Y_l^m(\mathbf{u}) - \frac{1}{\sqrt{4\pi}}c_{00}\right|^2 d\mathbf{u} \\
&= \frac{1}{4\pi}\int_{S^2}\left|\sum_{l=0}^{\infty}\sum_{m=-l}^{l} c_{lm}Y_l^m(\mathbf{u}) - c_{00}Y_0^0(\mathbf{u})\right|^2 d\mathbf{u} \\
&= \frac{1}{4\pi}\int_{S^2}\left|\sum_{l=1}^{\infty}\sum_{m=-l}^{l} c_{lm}Y_l^m(\mathbf{u})\right|^2 d\mathbf{u} \\
&= \frac{1}{4\pi}\int_{S^2}\left[\sum_{l=1}^{\infty}\sum_{m=-l}^{l} c_{lm}Y_l^m(\mathbf{u})\right]\left[\sum_{l'=1}^{\infty}\sum_{m'=-l'}^{l'} c_{l'm'}Y_{l'}^{m'}(\mathbf{u})\right] d\mathbf{u} \\
&= \frac{1}{4\pi}\sum_{l=1}^{\infty}\sum_{m=-l}^{l}\sum_{l'=1}^{\infty}\sum_{m'=-l'}^{l'} c_{lm}c_{l'm'}\delta_{lm}^{l'm'} \\
&= \frac{1}{4\pi}\sum_{l=1}^{\infty}\sum_{m=-l}^{l}[c_{lm}]^2.
\end{aligned} \tag{11}$$

Since the well known power-spectrum invariants for each degree, l, is

$$I_l[f] = \sum_{m=-l}^{l}[c_{lm}]^2 \tag{12}$$

we can express the variance invariant in Eq. (11) as the sum of power-spectrum invariants, $I_l[f]$, at different degree l:

$$I_{variance}[f] = \frac{1}{4\pi} \sum_{l=1}^{\infty} I_l[f]. \tag{13}$$

As in the case of the mean, the calculation of this invariant also involves an *integral* but in this case we integrate the square of the function. Power-spectrum invariants have been used in dMRI to improve the microstructural indexes estimation in Novikov et al. (2018b) and Reisert et al. (2016).

2.3. Volume of the signal and bispectrum invariants

The third intuitive invariant that we are considering is the volume. The volume of a spherical function (Baxansky and Kiryati, 2007) can be calculated as

$$\begin{aligned} I_{volume}[f] &= \int_{S^2} \int_{\varphi=0}^{f(\mathbf{u})} \varphi^2 d\varphi \; d\mathbf{u} \\ &= \frac{1}{3} \int_{S^2} [f(\mathbf{u})]^3 \, d\mathbf{u} \end{aligned} \tag{14}$$

which for the SH expansion of $f(\mathbf{u})$ leads to[3]

$$\begin{aligned} I_{volume}[f] &= \frac{1}{3} \int_{S^2} [f(\mathbf{u})]^3 \, d\mathbf{u} \\ &= \frac{1}{3} \int_{S^2} \left[\sum_{l=0}^{\infty} \sum_{m=-l}^{l} c_{lm} Y_l^m(\mathbf{u}) \right]^3 d\mathbf{u} \\ &= \frac{1}{3} \int_{S^2} \sum_{l_1,m_1} \sum_{l_2,m_2} \sum_{l_3,m_3} c_{l_1 m_1} c_{l_2 m_2} c_{l_3 m_3} Y_{l_1}^{m_1}(\mathbf{u}) Y_{l_2}^{m_2}(\mathbf{u}) Y_{l_3}^{m_3}(\mathbf{u}) d\mathbf{u} \\ &= \frac{1}{3} \sum_{l_1,m_1} \sum_{l_2,m_2} \sum_{l_3,m_3} c_{l_1 m_1} c_{l_2 m_2} c_{l_3 m_3} \int_{S^2} Y_{l_1}^{m_1}(\mathbf{u}) Y_{l_2}^{m_2}(\mathbf{u}) Y_{l_3}^{m_3}(\mathbf{u}) d\mathbf{u} \\ &= \frac{1}{3} \sum_{l_1,m_1} \sum_{l_2,m_2} \sum_{l_3,m_3} c_{l_1 m_1} c_{l_2 m_2} c_{l_3 m_3} G(l_1, m_1 | l_2, m_2 | l_3, m_3) \end{aligned} \tag{15}$$

[3] In all the equations involving multiple SH summations we will use the following notation: $\sum_{l,m} = \sum_{l=0}^{\infty} \sum_{m=-l}^{l}$.

where G represents the Gaunt coefficient calculated as the integral of three real SH as explained by Homeier and Steinborn (1996). There is a remarkable similarity between the volume equation (15) and the bispectrum invariants proposed by Kondor (2007)

$$I^{bispectrum}_{l_1,l_2,l_3}[f] = \sum_{m_1=-l_1}^{l_1} \sum_{m_2=-l_2}^{l_2} \sum_{m_3=-l_3}^{l_3} c_{l_1 m_1} c_{l_2 m_2} c_{l_3 m_3} C(l_1, m_1 | l_2, m_2 | l_3, m_3) \tag{16}$$

where C are the *Clebsch-Gordan coefficients*. Given the relationship between Gaunt and Clebsch-Gordan coefficients

$$G(l_1, m_1 | l_2, m_2 | l, m) = \sqrt{\frac{(2l_1+1)(2l_2+1)}{(2l+1)}} C(l_1, 0 | l_2, 0 | l, 0) C(l_1, m_1 | l_2, m_2 | l, m) \tag{17}$$

we can express the volume of $f(\mathbf{u})$ as

$$I_{volume}[f] = \frac{1}{3} \sum_{l_1=0}^{\infty} \sum_{l_2=0}^{\infty} \sum_{l_3=0}^{\infty} I^{bispectrum}_{l_1,l_2,l_3}[f] \sqrt{\frac{(2l_1+1)(2l_2+1)}{(2l_3+1)}} C(l_1, 0 | l_2, 0 | l_3, 0). \tag{18}$$

As in the case of the variance, it is possible to split an invariant, the volume in this case, as the sum of multiple bispectrum invariants for each degree set $[l_1, l_2, l_3]$. In this case, the calculation of the invariant involves the calculation of the integral of the function cubed. To our knowledge, the bispectrum invariants and the volume have not been used in dMRI. In Section 5, we will apply these invariants to the dMRI signal for the first time.

2.4. A general framework for the generation of invariants

We can generalize the mean, variance, and volume equations by considering the integral of a spherical function $f(\mathbf{u})$ elevated to an integer power d:

$$\begin{aligned} I_d[f] &= \int_{S^2} [f(\mathbf{u})]^d \, d\mathbf{u} \\ &= \int_{S^2} \left[\sum_{l=0}^{\infty} \sum_{m=-l}^{l} c_{lm} Y_l^m(\mathbf{u}) \right]^d d\mathbf{u} \\ &= \int_{S^2} \sum_{l_1,m_1} \cdots \sum_{l_d,m_d} c_{l_1 m_1} \cdots c_{l_d m_d} Y_{l_1}^{m_1}(\mathbf{u}) \cdots Y_{l_d}^{m_d}(\mathbf{u}) d\mathbf{u} \\ &= \sum_{l_1,m_1} \cdots \sum_{l_d,m_d} c_{l_1 m_1} \cdots c_{l_d m_d} \int_{S^2} Y_{l_1}^{m_1}(\mathbf{u}) \cdots Y_{l_d}^{m_d}(\mathbf{u}) d\mathbf{u} \\ &= \sum_{l_1 \ldots l_d} \cdots \sum_{m_1 \ldots m_d} c_{l_1 m_1} \cdots c_{l_d m_d} G(l_1, m_1 | \cdots | l_d, m_d) \end{aligned} \tag{19}$$

where G in this case represents the generalized Gaunt coefficients, namely the integral of d SH (Homeier and Steinborn, 1996). We can easily prove that this function is always an RIF given that

$$I_d[f] = \int_{S^2} [f(\mathbf{u})]^d \, d\mathbf{u} = \int_{S^2} \left[f(\mathbf{R}^{-1}\mathbf{u}) \right]^d d\mathbf{u} \tag{20}$$

for any d. The structure of Eq. (19) is similar to variance equation (11) and volume equation (15). Therefore, considering $\mathbf{l} = [l_1, l_2 \cdots, l_d]$, it makes sense to define a new set of invariants calculated as

$$I_{\mathbf{l}}[f] = \sum_{m_1=-l_1}^{l_1} \cdots \sum_{m_d=-l_d}^{l_d} c_{l_1 m_1} \cdots c_{l_d m_d} G(l_1, m_1 | \cdots | l_d, m_d). \tag{21}$$

While we can perceive by analogy that $I_{\mathbf{l}}[f]$ is an RIF, Appendix A provides a formal proof that Eq. (21) will always produce an RIF given any set of $\mathbf{l}$.

2.5. A maximal subset of algebraic independent invariants

We have proved (see Appendix A) that $I_{\mathbf{l}}[f]$ represents an RIF for any considered $\mathbf{l} = [l_1 \ldots l_d]$. However, given two invariants $I_{\mathbf{l}_1}[f]$ and $I_{\mathbf{l}_2}[f]$ with $\mathbf{l}_1 \neq \mathbf{l}_2$, these two invariants may be identical or dependent of each other. The goal of this section is to find the maximal set of invariants which are *algebraically*

L	$d=1$	$d=2$	$d=3$	$d=4$	$d=5$
2	1 (**1**)	2 (**2**)	3 (**3***)	4 (**3***)	5 (**3***)
4	1 (**1**)	3 (**3**)	7 (**7**)	12 (**11**)	18 (**12***)
6	1 (**1**)	4 (**4**)	13 (**13**)	28 (**25***)	49 (**25***)
8	1 (**1**)	5 (**5**)	35 (**22**)	70 (**42***)	126 (**42***)

Table 1: Number of invariants for real symmetric SH basis given the maximum degree L and power d. In bold we report the number of algebraically independent invariants with an asterisk if the number corresponds to the maximum theoretical number of algebraic independent invariants for the truncation degree L considered in the line.

independent. This means that every element of a set of independent invariants cannot be written as an algebraic function of the other invariants in the set.

First we noticed that $I_{\mathbf{l}}[f]$ is equal to zero for a large subset of $\mathbf{l}$. This is explained by the fact that the space of the real Gaunt coefficients themselves is very sparse and the coefficients are mostly zero. A simple example of this arises when considering the case where $d = 2$ and truncation degree, $L = 2$. The complete list of invariants is $\left[I_{0,0}, I_{0,1}, I_{0,2}, I_{1,0}, I_{1,1}, I_{1,2}, I_{2,0}, I_{2,1}, I_{2,2}\right]$. However, because $G(l_1, m_1|l_2, m_2) = \delta_{l_1,m_1}^{l_2,m_2}$ all the mixed terms will be zero. The non-zero invariants that are left $\left[I_{0,0}, I_{1,1}, I_{2,2}\right]$ correspond to the power-spectrum invariants.

A second property of the Gaunt coefficients is that they are invariant to a permutation of the indexes l and m. Therefore, the invariant $I_{2,2,4}$ is equal to $I_{2,4,2}$ and $I_{4,2,2}$. A separate note should be made concerning the evolution of the invariant with the power d. Take, for instance, the simplest case of the invariants: I_0, $I_{0,0}$, and $I_{0,0,0}$ for $d = 1$, $d = 2$, and $d = 3$ respectively. In this case we have: $I_0[f] = c_{00}\sqrt{4\pi}$, $I_{0,0}[f] = c_{00}^2$, and $I_{0,0,0}[f] = c_{00}^3 \frac{1}{\sqrt{4\pi}}$. As we can see, these invariants are not algebraically independent: the $d = 2$ and $d = 3$ invariants are simply powers of the $d = 1$ invariant.

In general, we say a set of polynomials – whose variables X are the SH coefficients – is algebraically independent if the following definition holds (Caruyer and Verma, 2015).

Definition. *A set of m polynomials $P_1, \ldots, P_m \in R[X_1, \ldots, X_n]$ are called algebraically independent over the field R if*

$$\forall Q \in R[Y_1, \ldots, Y_m], \qquad Q(P_1, \ldots, P_m) = 0 \iff Q = 0$$

Example *Given $P_1 = 2x^2 - 4xy + 2y^2$ and $P_2 = x - y$, the set $[P_1, P_2]$* is not *algebraically independent. In fact, considering $Q = 2P_2^2 - P_1$ it leads to: $2(x-y)^2 - (2x^2 - 4xy + 2y^2) = 0$.*

We are interested in finding a maximal subset of algebraically independent non-zero RIF, given the truncated SH maximum degree L and the maximal power d. A computationally efficient way to verify whether a set of invariants $I_{\mathbf{l}}$ are algebraically independent is the Jacobian theorem (Ehrenborg and Rota, 1993):

Theorem 1. *The polynomials $P_1, \ldots, P_m \in R[X_1, \ldots, X_n]$ with $m \leq n$ are algebraically independent iff the Jacobian matrix $\boldsymbol{J} = (\partial P_i / \partial X_j)_{1 \leq i \leq m, 1 \leq j \leq n}$ has full rank.*

In this case, the Jacobian is composed by the partial derivatives of our invariants $I_{\mathbf{l}}$ with respect to the coefficients c_{lm}. We test for full-rankness using the Schwartz-Zippel polynomial identity testing lemma (Zippel, 1979; Schwartz, 1980) for the Jacobian matrix (Kayal, 2009):

Theorem 2. *Let $C = [c_1, c_2, \ldots, c_n]$ be selected random independently and uniformly from the field S. Then*

$$\mathbb{P}\Big(rank\,(\boldsymbol{J}(P_1 \ldots P_m)|_{X=C}) \neq rank\,(\boldsymbol{J}(P_1 \ldots P_m)) \Big) \leq \tfrac{d}{|S|}$$

where d is the degree of the polynomial.

This means that given a random vector of coefficients C, the rank of the Jacobian corresponds to the rank of $(\partial P_i / \partial X_j)_{X=C}$ with a probability proportional to the probability of the random extraction of C. For this work, we tried 100 instances of C in order to verify the independence of a set $I_{\mathbf{l}}$. Given the fact that $|S|$ corresponds to the number of distinct floating-point vectors of length n

L	$d=1$	$d=2$	$d=3$	$d=4$
2	1 (**1**)	3 (**3**)	5 (**5**)	8 (**6***)
3	1 (**1**)	4 (**4**)	8 (**8**)	17 (**13***)
4	1 (**1**)	5 (**5**)	14 (**14**)	33 (**22***)
5	1 (**1**)	6 (**6**)	20 (**20**)	57 (**33***)
6	1 (**1**)	7 (**7**)	30 (**30**)	94 (**46***)
7	1 (**1**)	8 (**8**)	120 (**40**)	330 (**61***)
8	1 (**1**)	9 (**9**)	165 (**55**)	495 (**78***)

Table 2: Number of invariants for real SH basis given the maximum degree L and power d. In bold we report the number of algebraically independent invariants with an asterisk if the number corresponds to the maximum theoretical number of algebraic independent invariants for the truncation degree L considered in the line.

the probability of the rank to be incorrect is basically zero. This approach has been previously used by Caruyer and Verma (2015) for the same purpose. The number of algebraically independent invariants is equal to $n_c - 3$, where n_c is the number of SH coefficients used and three are the degrees of freedom of the rotation (Ghosh et al., 2012a; Caruyer and Verma, 2015). For the symmetric SH basis $n_c = \frac{(L+1)(L+2)}{2}$, while for the complete SH basis $n_c = (L+1)^2$, where L is the truncation degree of the considered SH basis. Table 1 show the number of invariants calculated for the symmetric SH basis Descoteaux et al. (2007). We highlight the number of algebraically independent invariants in bold font marking it with an asterisk if this number corresponds to $n_c - 3$, the maximum number of algebraic independent invariant for a given L. For the real SH basis we noticed that considering $d = 4$ we are able to obtain all the algebraically independent invariants testing up to $L = 8$ (see table 2). For the symmetric SH basis, our framework requires $d = 5$ to generate all the 12 invariants for $L = 4$. The Caruyer and Verma (2015) framework was able to generate the 12 invariants for $L = 4$ at $d = 4$, as in the case of our framework for the complete SH basis. With our technique, the 12^{th} missing invariant at $d = 4$ appears as a function of even SH coefficients only at $d = 5$.

In this section, we were able to design a new computational framework for generating rotation invariants from the SH representation of spherical functions. We also proved that our framework is able to generate all the algebraically independent invariants up to degree $L = 8$. In the next section, we will analyze two possible dMRI applications of our rotation invariant framework. In the first application, we will link our new RIF to existing well established dMRI indexes. In the second application, we will investigate the sensitivity of our RIF to brain tissue microstructure.

3. dMRI application of the new invariants

3.1. RIF of the Apparent Diffusion Coefficient

The ADC profile [4] represents the apparent value of the diffusivity coefficient D in the direction modeled by the unit vector $\mathbf{u}$. It can be calculated via the expression

$$E(\mathbf{b}) = \exp(-bD(\mathbf{u})) \tag{22}$$

where E is the normalized[5] diffusion signal, $\mathbf{b} = b\mathbf{u}$ is the *b-vector*, and $D(\mathbf{u})$ is the ADC in the direction $\mathbf{u}$. Historically, the most common way to model the ADC has been to consider the dMRI signal as Gaussian, modeling $D(\mathbf{u})$ as a Rank-2 positive definite tensor $\mathbf{D}$

$$D(\mathbf{u}) = \mathbf{u}^T\mathbf{D}\mathbf{u}. \tag{23}$$

In this case, the ADC represents the covariance matrix $\mathbf{D}$ of the Gaussian signal. Substituting Eq. (23) into Eq. (22) we obtain the signal equation of the popular Diffusion Tensor Imaging (DTI) model, from Basser et al. (1994):

$$E(\mathbf{b}) = \exp(-b\mathbf{u}^T\mathbf{D}\mathbf{u}). \tag{24}$$

[4] In some of the earlier works, the Mean Diffusivity has also been called ADC mainly because the acquisition at the time did not have enough samples to characterize the complete ADC profile.

[5] The diffusion signal is normalized when $E(0) = 1$.

One of the most important advantages of the diffusion tensor is that its eigenvalues and eigenvectors decomposition can be related to diffusion properties of the tissues

$$\mathbf{D} = \lambda_1 \mathbf{v}_1 \mathbf{v}_1^T + \lambda_2 \mathbf{v}_2 \mathbf{v}_2^T + \lambda_3 \mathbf{v}_3 \mathbf{v}_3^T \tag{25}$$

with λ_i the i^{th} biggest eigenvalue associated to the eigenvector $\mathbf{v}_i$. The eigenvector $\mathbf{v}_1$, associated with the biggest eigenvalue λ_1, corresponds to the main diffusion direction in the tissue. In white matter voxel this direction corresponds to the average axons main axis. The associated eigenvalue λ_1 represents the ADC in the principal diffusion direction.

In general, we can use SH in order to rewrite $D(\mathbf{u})$ as the symmetric SH series

$$D(\mathbf{u}) = \sum_{l=0,even}^{L} \sum_{m=-l}^{l} c_{lm} Y_l^m(\mathbf{u}). \tag{26}$$

In the case of a rank-2 tensor the ADC can be rewritten as

$$\begin{aligned} D(\mathbf{u}) =& \mathbf{u}^T \mathbf{D}(\mathbf{v}) \mathbf{u} \\ =& \mathbf{u}^T \left[\lambda_1 \mathbf{v}_1 \mathbf{v}_1^T + \lambda_2 \mathbf{v}_2 \mathbf{v}_2^T + \lambda_3 \mathbf{v}_3 \mathbf{v}_3^T \right] \mathbf{u} \\ =& \lambda_1 \mathbf{u}^T \mathbf{v}_1 \mathbf{v}_1^T \mathbf{u} + \lambda_2 \mathbf{u}^T \mathbf{v}_2 \mathbf{v}_2^T \mathbf{u} + \lambda_3 \mathbf{u}^T \mathbf{v}_3 \mathbf{v}_3^T \mathbf{u} \\ =& \lambda_1 (\mathbf{u}^T \mathbf{v}_1)^2 + \lambda_2 (\mathbf{u}^T \mathbf{v}_2)^2 + \lambda_3 (\mathbf{u}^T \mathbf{v}_3)^2 \end{aligned} \tag{27}$$

and the corresponding SH coefficients can be obtained as

$$\begin{aligned} c_{lm} &= \int_{S^2} \left[\lambda_1 (\mathbf{u}^T \mathbf{v}_1)^2 + \lambda_2 (\mathbf{u}^T \mathbf{v}_2)^2 + \lambda_3 (\mathbf{u}^T \mathbf{v}_3)^2 \right] Y_l^m(\mathbf{u}) d\mathbf{u} \\ &= \sum_{i=1}^{3} \int_{S^2} \lambda_i (\mathbf{u}^T \mathbf{v}_i)^2 Y_l^m(\mathbf{u}) d\mathbf{u} \\ &= \sum_{i=1}^{3} \lambda_i 2\pi \int_{-1}^{1} P_l(t) t^2 dt \; Y_l^m(\mathbf{v}_i). \end{aligned} \tag{28}$$

Due to the Funk-Hecke theorem (see Supplementary Material Section 2), the integral $\int_{-1}^{1} P_l(t) t^2 dt$ results in

$$\int_{-1}^{1} P_l(t) t^2 dt = \begin{cases} \frac{2}{3}, & \text{if } l = 0 \\ \frac{4}{15}, & \text{if } l = 2 \\ 0, & \text{if } l \geq 4 \end{cases} \tag{29}$$

leading to

$$c_{00} = \frac{\sqrt{4\pi}}{3}(\lambda_1+\lambda_2+\lambda_3) \quad (30)$$

$$c_{2m} = \frac{8\pi}{15}\sum_{i=1}^{3}\lambda_i Y_2^m(\mathbf{v}_i). \quad (31)$$

Therefore, for DTI ADC model, we have $L = 2$, with for the even SH basis results to $n_c = 6$ SH coefficients. We know from Table 1 that in this case we have three algebraically independent invariants: one at $d = 1$, one at $d = 2$, and the last at $d = 3$. Substituting Eq. (30) and Eq. (31) into Eq. (21) we obtain the following:

$$I_0[D] = \frac{4\pi}{3}(\lambda_1+\lambda_2+\lambda_3) \quad (32)$$

$$I_{22}[D] = \frac{8\pi}{45}\left[(\lambda_1-\lambda_2)^2+(\lambda_1-\lambda_3)^2+(\lambda_2-\lambda_3)^2\right] \quad (33)$$

$$I_{222}[D] = \frac{32\pi}{945}\Big[2\big(\lambda_1^3+\lambda_2^3+\lambda_3^3\big)-3\big(\lambda_1^2\lambda_2+\lambda_1^2\lambda_3+\lambda_1\lambda_2^2+\lambda_1\lambda_3^2+ \quad (34)$$
$$+\lambda_2^2\lambda_3+\lambda_2\lambda_3^2\big)+12\lambda_1\lambda_2\lambda_3\Big].$$

See Supplementary Material Section 4 for a detailed explanation on the calculation of the invariants. It should be noted that two of the principal DTI invariants classically used in literature – Mean Diffusivity (MD) and Fractional Anisotropy (FA) – can be derived from our RIF:

$$MD = \frac{I_0[D]}{4\pi} \quad (35)$$

$$FA = \sqrt{\frac{3}{2}\frac{10\pi I_{22}[D]}{I_0[D]^2+10\pi I_{22}[D]}}. \quad (36)$$

The volume as well can be obtained from an algebraic combination of the RIFs by substituting Eq. (30) and Eq. (31) into Eq. (15):

$$I_{volume}[D] = \frac{1}{3}\left[\frac{I_0[D]^3}{(4\pi)^2}+\frac{3}{4\pi}I_0[D]I_{22}[D]+I_{222}[D]\right]. \quad (37)$$

Using a rank-2 tensor for modeling the ADC assumes that the water molecules displacement in the tissues follows a Gaussian distribution. However, the dMRI signal in white matter has been shown to be non Gaussian not only in voxel

containing crossing of fibers but also in single fiber bundle voxels (Santis et al., 2011). In order to overcome this limitation, high-rank tensor models have been proposed (Frank, 2002; Özarslan and Mareci, 2003; Özarslan et al., 2005; Schultz et al., 2014). Fitting high-rank model can also provide some insight into the quantification of the non-Gaussianity of the diffusion signal. In fact, for Gaussian signal, only SH coefficients with $l \leq 2$ will be non-zero. Hence, a positive energy for $l = 4$, for example, may be an interesting clue for the presence of multiple tissue compartments in the considered voxel (Frank, 2002; Özarslan et al., 2005). However, a high level of noise may produce spurious non-zero high-degree SH coefficients, therefore, such a result should be taken with caution.

3.2. RIF of the dMRI signal and the fODF

The diffusion signal itself, for a given b-value, can be expressed as a spherical function. Therefore, we can directly calculate its SH-series expansion as

$$E(b, \mathbf{u}) = \sum_{l=0,even}^{L} \sum_{m=-l}^{l} a_{lm}(b) Y_l^m(\mathbf{u}). \tag{38}$$

In this case the SH coefficients a_{lm} depend on the b-value; for a different shell we will obtain a different set of coefficients.

Several dMRI signal models (Kaden et al., 2016a; Zucchelli et al., 2017; Novikov et al., 2018a; Reisert et al., 2016) assume that the diffusion signal generated by a single bundle of fibers all coherently aligned in the direction marked by the unit vector $\mathbf{v}$ – also known as fiber response function (FRF) – can be expressed as a sum of axially symmetric Gaussians

$$E_{FRF}(b, \mathbf{u}|\mathbf{v}) = \sum_{i}^{C} \nu_i \exp\left(-b\left[(\lambda_{\parallel,i} - \lambda_{\perp,i})(\mathbf{u}^T\mathbf{v})^2 + \lambda_{\perp,i}\right]\right) \tag{39}$$

where C is the number of compartments and ν_i, $\lambda_{\parallel,i}$ and $\lambda_{\perp,i}$ are, respectively, the signal volume fraction, parallel and perpendicular diffusivity of the i^{th} compartment. Assuming the fiber population in a given voxel is homogeneous but not coherently aligned, we can calculate the diffusion signal $E(\mathbf{b})$ as the convolution of the single fiber response E_{FRF} with the fODF $\rho(\mathbf{v})$

$$E(b, \mathbf{u}) = \int_{S^2} E_{FRF}(b, \mathbf{u}|\mathbf{v})\rho(\mathbf{v})d\mathbf{v}. \tag{40}$$

The fODF gives the probability of having a fiber in the direction $\mathbf{v}$. It is antipodally symmetric, non-negative, and its integral is unity. We can model fODF as a SH expansion

$$\rho(\mathbf{v}) = \sum_{l=0,even}^{L} \sum_{m=-l}^{l} c_{lm} Y_l^m(\mathbf{v}). \tag{41}$$

Substituting Eq. (39) and Eq. (41) into Eq. (40) we obtain the following expression

$$E(b, \mathbf{u}) = \sum_{l=0,even}^{L} \sum_{m=-l}^{l} c_{lm} K_l(b, \mathbf{p}) Y_l^m(\mathbf{u}) \tag{42}$$

where the microstructural kernel $K_l(b, \mathbf{p})$ will depend on the number of compartments and the parameters vector $\mathbf{p} = [\nu_1, \lambda_{\parallel,1}, \lambda_{\perp,1}, \ldots, \nu_C, \lambda_{\parallel,C}, \lambda_{\perp,C}]$ (see Supplementary Material Section 5 for the complete derivation of the kernel). Comparing Eq. (42) to Eq. (38) we obtain the identity

$$\sum_{l=0,even}^{L} \sum_{m=-l}^{l} a_{lm}(b) Y_l^m(\mathbf{u}) = \sum_{l=0,even}^{L} \sum_{m=-l}^{l} c_{lm} K_l(b, \mathbf{p}) Y_l^m(\mathbf{u}). \tag{43}$$

Substituting Eq. (43) in the invariants equation, Eq. (21) we derive that

$$I_{\mathbf{l}}[E] = I_{\mathbf{l}}[\rho] \prod_{l_i \in \mathbf{l}} K_{l_i}(b, \mathbf{p}). \tag{44}$$

Thus, an invariant on the signal at a given b-value is equal to the same invariant calculated for the fODF times the product of the microstructural kernel at different l. Eq. (44) is a generalization of the SMT (Kaden et al., 2016a) and the *Rot Inv* framework (Novikov et al., 2018a). For example in the case of the SMT we obtain

$$\begin{aligned} I_0[E] &= I_0[\rho] K_0(b, \mathbf{p}) \\ &= K_0(b, \mathbf{p}) \end{aligned} \tag{45}$$

since $I_{\mathbf{0}}[\rho] = 1$ for any fODF[6]. In the case of the *Rot Inv* framework for the

[6] $I_{\mathbf{0}} = \sqrt{4\pi} c_{00}$. Because the integral of the fODF is one, we have $c_{00} = \frac{1}{\sqrt{4\pi}}$. Therefore, $I_{\mathbf{0}}[\rho] = 1$.

power-spectrum invariant I_{22} we obtain

$$\begin{aligned} I_{22}[E] &= I_{22}[\rho] \prod_{l_i \in [2,2]} K_{l_i}(b, \mathbf{p}) \\ &= I_{22}[\rho] \left[K_2(b, \mathbf{p})\right]^2 . \end{aligned} \tag{46}$$

We can use Eq. 44 for multiple $\mathbf{l}$ in order to create a system of equations in which the signal invariants at different b-values $I_{\mathbf{l}}[E]$ are the known terms, and the fODF invariants $I_{\mathbf{l}}[\rho]$ and the microstructural parameters $\mathbf{p}$ are the unknowns. Given $\mathcal{L}$, the considered set of invariants, n_b the number of shells, and n_p the number of microstructural parameters, the number of known terms is $|\mathcal{L}| \times n_b$ while the number of unknowns is $|\mathcal{L}| + n_p$. Therefore, if the number of shells n_b is large enough the system will be overdetermined and an approximate solution can be found using non-linear optimization methods.

We can identify two special cases of fODF which impact the invariants. The first case arises when the fODF is uniformly distributed. In this case all $I_{\mathbf{l}}[\rho]$ with $\mathbf{l} \neq 0$ will be zero, therefore, only $I_0[E]$ can be used for the fitting. The second case arises when the fODF is a Dirac's delta function δ, namely when fibers are all aligned in a single coherent direction. In this case, the fODF invariants $I_{\mathbf{l}}[\rho]$ appear to be maximum (see Supplementary Material Section 3). For Dirac's deltas the fODF coefficients are equal to the SH basis evaluated in the direction of the fibers $\mathbf{v}$: $c_{lm} = Y_{lm}(\mathbf{v})$. We can thus define the normalized fODF invariants as

$$\hat{I}_{\mathbf{l}}[\rho] = \frac{I_{\mathbf{l}}[\rho]}{I_{\mathbf{l}}[\delta]}. \tag{47}$$

where $\hat{I}_{\mathbf{l}}[\rho]$ have the advantage of being bounded in $[-1, 1]$. The same normalization can be applied to the signal invariants and it is useful to both the visualization of the invariants and the fitting of the microstructural parameters vector.

4. Materials and Methods

4.1. In-vivo data

In order to test our new invariants in-vivo, we select 44 subjects of the Human Connectome Project (HCP) diffusion MRI test-retest dataset[7] (Sotiropoulos et al., 2013) for a total of 88 subjects. The HCP acquisition protocol is composed of 18 b-value 0 s/mm^2 volumes, and 90 volumes at b-values 1000, 2000, and 3000 s/mm^2, respectively. The gradient directions in the three shells were computed using the algorithm proposed by Caruyer et al. (2013) which guarantees uniform angular coverage. HCP pulse separation time and pulse width are $\Delta = 43.1$ms and $\delta = 10.6$ms, respectively. Each volume is composed of $145 \times 174 \times 145$ voxels with a $1.25 \times 1.25 \times 1.25$ mm^3 resolution. HCP dataset provides also a T1 based white matter segmentation for each brain extracted using freesurfer[8] (Fischl et al., 2002).

We use SH of degree $L = 4$ for fitting the HCP data, considering all the coefficients while fitting the signal and only the coefficients up to $l = 2$ for the ADC. We fit the spherical signal using least squares method with Laplace-Beltrami regularization as in Descoteaux et al. (2007) with regularization parameter set to 0.01.

4.2. Synthetic data

In this work, we consider two sets of synthetic data. In the first data set, we consider the simple case of the crossing of two fiber bundles, each of them perfectly aligned with no internal dispersion and with a volume fraction of 0.5 for each bundle. The two bundles directions were randomly picked, in order to have randomly oriented bundles and crossing angles. One thousand different fiber configurations were considered for this data set. We simulate the diffusion signal using Eq. (42) given the SH coefficients corresponding to the considered crossing fibers and a single fiber response representing a single compartment

[7] `https://www.humanconnectome.org/`

[8] `https://surfer.nmr.mgh.harvard.edu/`

with parallel diffusivity $\lambda_{\parallel} = 1.7 \times 10^{-3}$ mm^2/s and a perpendicular diffusivity $\lambda_{\perp} = 0.3 \times 10^{-3}$ mm^2/s.

In the second data set, we try to emulate white matter bundles in order to investigate a more realistic scenario. In this case we still consider crossings of two bundles with random orientation but, for this second dataset, each bundle is modeled with a Watson distribution (Alexander et al., 2010) with dispersion parameter, κ, randomly picked from a truncated Gaussian distribution with $\mu = 16$ and $\sigma = 2$. Only values in the interval $\kappa = [0, 128]$ were considered for this dataset and each of the two bundles of the synthetic voxel have the same κ. We model the single fiber response using a two compartments model having the same parallel diffusivity $\lambda_{\parallel,1} = \lambda_{\parallel,2}$ but different perpendicular diffusivity $\lambda_{\perp,1} \neq \lambda_{\perp,2}$. In particular we consider the first compartment as a stick $\lambda_{\perp,1} = 0$ mm^2/s modeling the intra-axonal water and the second compartment as an axially symmetric tensor modeling the extra-axonal water. As for the dispersion parameter, we picked the values of the intra-axonal compartment volume fraction ν_{ia}, the parallel diffusivity, and the extra-axonal perpendicular diffusivity from a truncated Gaussian distribution. The considered values were $\nu_{ia} \in [0.5, 1.0]$ with $\mu = 0.75$ and $\sigma = 0.1$, $\lambda_{\parallel} \in [1.5, 2.5] \times 10^{-3}$ mm^2/s with $\mu = 2.0 \times 10^{-3}$ mm^2/s and $\sigma = 0.1 \times 10^{-3}$ mm^2/s, and $\lambda_{\perp} \in [0.3, 1.0] \times 10^{-3}$ mm^2/s with $\mu = 0.5 \times 10^{-3}$ mm^2/s and $\sigma = 0.05 \times 10^{-3}$ mm^2/s. Finally, we add Rician noise with a signal to noise ratio of 30 in each synthetic voxel. For this second data set, we created a total of 1000 synthetic voxels. For this synthetic data set we considered 10 shells with b-values equally spaced from 1000 s/mm^2 to 10000 s/mm^2, with 60 directions per shell plus 30 samples at b=0 s/mm^2. We use SH of degree 4 to model the data, with Laplace-Beltrami regularization as for the HCP data.

4.3. Microstructural parameters estimation

For each voxel in the synthetic and in-vivo data we aim to retrieve three microstructural parameters: the intra-axonal volume fraction ν_{ia}, the parallel diffusivity $\lambda_{\parallel}$, and the extra-axonal perpendicular diffusivity $\lambda_{\perp}$. To do this,

we first calculate the 12 normalized algebraic independent invariants for SH of degree 4 for each of the three b-values, $\hat{I}_{\mathbf{l}}[E(b)]$. This results in $12\times3 = 36$ known signal RIF linked to the unknown normalized fODF RIF and microstructural parameter vector $\mathbf{p} = [\nu_{ia}, \lambda_{\parallel}, \lambda_{\perp}]$ by

$$\hat{I}_{\mathbf{l}}[E(b)] = \hat{I}_{\mathbf{l}}[\rho] \prod_{l_i \in \mathbf{l}} K_{l_i}(b, \mathbf{p}) \tag{48}$$

which corresponds to Eq. (44) for normalized invariants. Given that $\hat{I}_0[\rho]$ is constant, the number of unknowns corresponds to 3 (the number of microstructural parameters) plus the number of considered invariants minus one. We use python least squares minimization package[9] in order to minimize the following criterion

$$\min_{\hat{I}_{\mathbf{l}}[\rho], \mathbf{p}} \sum_{b} \sum_{\mathbf{l} \in \mathcal{L}} \left| \hat{I}_{\mathbf{l}}[E(b)] - \hat{I}_{\mathbf{l}}[\rho] \prod_{l_i \in \mathbf{l}} K_{l_i}(b, \mathbf{p}) \right|^2 . \tag{49}$$

The following priors were used to initialize the fitting: $\nu_{ia} = 0.7$, $\lambda_{\parallel} = 2.0\times10^{-3}$ mm^2/s, and $\lambda_{\perp} = 0.5\times10^{-3}$ mm^2/s. The fitting of ν_{ia} was constrained between 0 and 1.0, while the fitting of $\lambda_{\parallel}$ and $\lambda_{\perp}$ between 0 and 3.0×10^{-3} mm^2/s. We calculate the error in the microstructural parameters estimation as

$$relative\ error = \frac{|p_{GT} - p_{estimated}|}{p_{GT}} \tag{50}$$

where p is the considered microstructural parameter (ν_{ia}, $\lambda_{\parallel}$, or $\lambda_{\perp}$), p_{GT} indicates the ground truth value used to generate the signal and $p_{estimated}$ the one estimated using Eq. (49). We would like to point out that by minimizing the criterion given by Eq. (49) we are able to retrieve all the fODF invariants without explicitly estimate the fODF. In this way, we avoid the problem of enforcing non-negativity in the fODF (Tournier et al., 2007).

[9] `https://docs.scipy.org/doc/scipy/reference/generated/scipy.optimize.leastsq.html`

5. Results

5.1. ADC invariants in-vivo

Figure 1 shows the values of six ADC RIF calculated from the SH coefficients (with $L = 2$) from a coronal slice of the HCP data, namely, FA, MD, the volume, and the algebraic independent degree 2 RIF $I_0[D]$, $I_{22}[D]$, and $I_{222}[D]$. In this case, we used only the b=1000 s/mm^2 shell to calculate the ADC as it is normally done in classic DTI invariant estimation. As expected, the SH derived FA and MD maps calculated using Eq. (35) and Eq. (36) are perfectly equal to FA and MD maps calculated using DTI. Volume invariant, $I_{volume}[D]$, presents the highest values for voxel containing cerebrospinal fluid, which is coherent with the fact that the high diffusivity values of free water results in higher ADC volume. Gray matter voxels generally present the lowest volumes among all the brain tissues. In the white matter, we observe high volume values for single fiber bundles regions like the Corpus Callosum (CC) and the corticospinal tracts and lower values in crossing fiber regions like corona radiata. Breaking down the single RIF that compose the volume in Eq. 37 we have $I_0[D]$, $I_{22}[D]$, and $I_{222}[D]$. $I_0[D]$ map corresponds to the MD multiplied by 4π, therefore, these two invariants are perfectly equivalent. $I_{22}[D]$, similarly to FA, shows non-zero values only in the white matter anisotropic voxels with high contrast between single fibers regions and crossing fibers areas. $I_{222}[D]$ shows a similar but even more pronounced contrast. In fact, this RIF presents zero values in gray matter and cerebrospinal fluid, while reaching negative values in some crossing fibers voxel.

5.2. Signal invariants and microstructural features estimation

Figure 2 (top left) shows the 12 normalized algebraic independent invariants calculated on the fODF of the first synthetic dataset (see Section 4.2). Figure 2 (A, B, and C) shows the same set of invariants, this time calculated on the signal, at the three different b-values used for the dataset (solid lines b=1000 s/mm^2, point dashed lines b=2000 s/mm^2, and dashed lines b=3000 s/mm^2). Figure 2

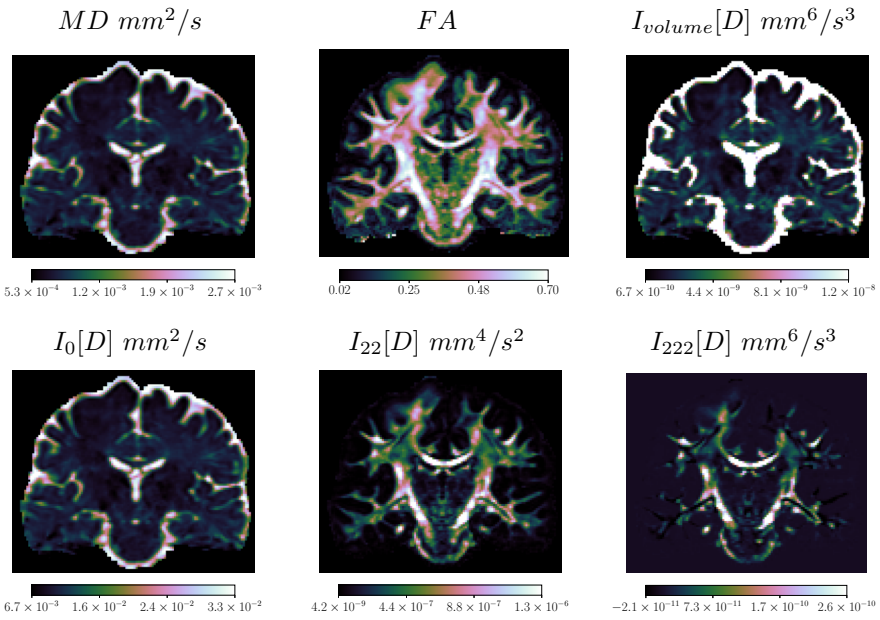

Figure 1: ADC invariants calculated on a coronal slice of one of the HCP subjects.

A (top right) shows the signal invariants $\hat{I}_0[E]$, $\hat{I}_{2,2}[E]$, and $\hat{I}_{2,2,2}[E]$. Figure 2 B (bottom left) shows the signal invariants $\hat{I}_{2,2,4}[E]$, $\hat{I}_{2,2,2,4}[E]$, and $\hat{I}_{2,2,2,2,4}[E]$. Finally, Figure 2 C (bottom right) shows the signal invariants $\hat{I}_{4,4}[E]$, $\hat{I}_{2,4,4}[E]$, $\hat{I}_{4,4,4}[E]$, $\hat{I}_{2,2,4,4}[E]$, $\hat{I}_{2,4,4,4}[E]$, and $\hat{I}_{4,4,4,4}[E]$. It is possible to see in all the graphs that all invariants are extremely sensitive to the crossing angle (excluding $\hat{I}_0$), although in different manners depending on the considered RIF. Signal invariants having a higher percentage of low-degree coefficients $l = 2$, such as $\hat{I}_{2,2}[E]$ and $\hat{I}_{2,2,2}[E]$, tend to have higher absolute values compared to invariants composed of many high-degree elements (e.g. $\hat{I}_{4,4,4}[E]$ and $\hat{I}_{4,4,4,4}[E]$). The b-value affects the invariants in a different manner depending on their degree-composition. For example, the amplitude of invariants in Figure 2 (A, low-degree invariants) decreases with the b-value. Conversely, the amplitude of invariants in Figure 2 (C, high-degree invariants) in general tends to increase with the b-value (e.g. $\hat{I}_{4,4}[E]$ and $\hat{I}_{4,4,4}[E]$). Mixed-degree invariants behave somewhere in between, having the highest amplitude at the intermediate b-

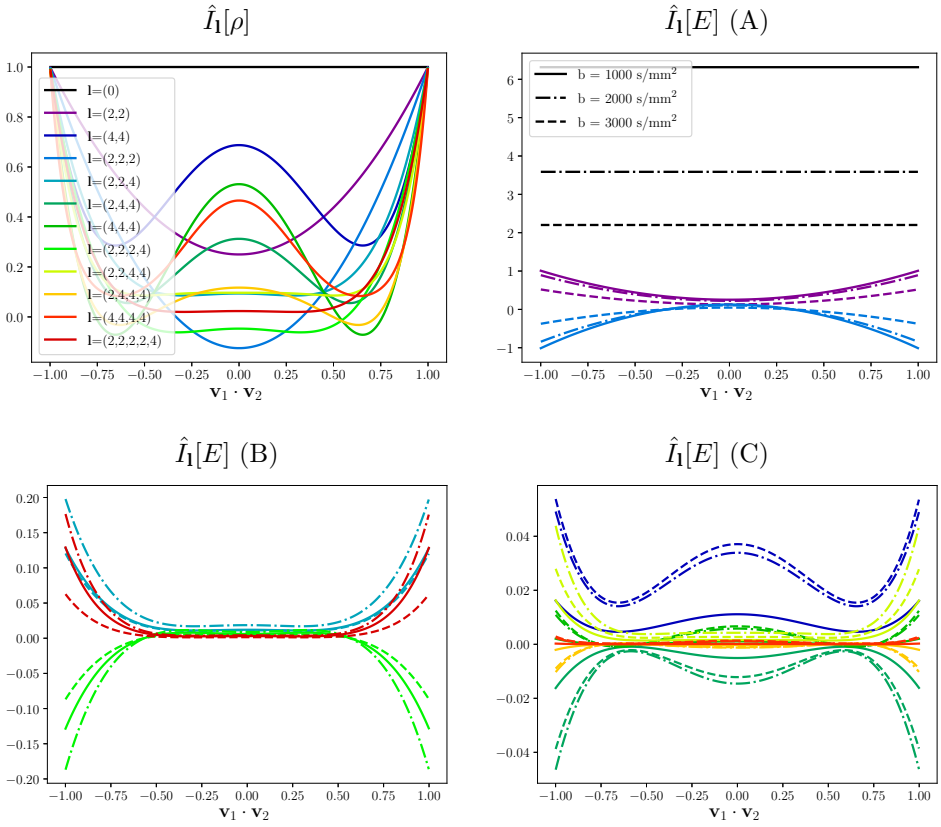

Figure 2: Simulation of the 12 algebraic independent invariants for SH degree 4 for crossing of two fibers aligned in the direction $\mathbf{v}_1$ and $\mathbf{v}_2$, respectively, in the fODF (top left) and in the signal (top right, bottom left, and bottom right).

value of 2000 s/mm^2. Although it is already known that shells with high b-values require SH of higher degree, the fact that our invariants capture this behavior so precisely is extremely interesting and can provide a useful tool to understand the advantage of higher b-values for brain microstructural feature estimation.

In order to test the added value of our invariants to the problem of tissue microstructure estimation, we tried to recover the microstructural parameters of the second synthetic data set as explained in Section 4.3 considering an increas-

ing number of invariants for the fitting. Initially, we test the microstructural parameter estimation using the RIF individually, in order to verify the microstructural sensitivity of each invariants. Therefore, we considered the fitting using a subset of the RIF which better performs individually (named as *selected*) in order to see if combining the best of our RIF we were able to improve the microstructural parameters estimation. In our preliminary (non presented) experiments we noticed that including all invariants was counterproductive because the poor performing invariants impacted negatively the global fitting. Eventually, we observed that only a small selection of the best performing invariants was able to improve the fitting.

Figure 3 reports the violin plots for the relative error of the fitting of ν_{ia} (top left), $\lambda_{\parallel}$ (top right), $\lambda_{\perp}$ (bottom left), and the average of the three (bottom right) for the 1000 voxels of the synthetic data set. The fitting of ν_{ia} in red appears to be sensitive to the use of $\hat{I}_0[E]$ (SMT), which obtains good performance in terms of fitting error. The other 11 RIF seems to be less accurate, in particular $\hat{I}_{222}[E]$ and $\hat{I}_{2224}[E]$ are the least sensitive to the intra-axonal volume fraction estimation. Concerning the fitting of $\lambda_{\parallel}$, degree 4 invariants $\hat{I}_{44}[E]$ and $\hat{I}_{4444}[E]$ show the best fitting error. As in the case of ν_{ia}, invariants $\hat{I}_{222}[E]$ and $\hat{I}_{2224}[E]$ have the worst performances. Perpendicular diffusivity estimation in Figure 3 (bottom left, in blue), is the only microstructural parameters in which $\hat{I}_0[E]$ performs poorly. Conversely, invariant $\hat{I}_{222}[E]$ in this case is one of the best, together with $\hat{I}_{22}[E]$ and $\hat{I}_{244}[E]$. Considering the average estimation error among all the parameters (bottom right), in purple, we were able to select the best performing sub-sample of RIF. The best performing selected invariants are $\hat{I}_0[E]$, $\hat{I}_{22}[E]$, $\hat{I}_{44}[E]$, $\hat{I}_{224}[E]$, $\hat{I}_{244}[E]$, $\hat{I}_{2244}[E]$, and $\hat{I}_{4444}[E]$. We selected these seven invariants considering not only the mean estimation error, but also its distribution, as well as specific sensitivity to a certain microstructural parameter (as in the case of $\hat{I}_0[E]$ for ν_{ia}). Combining the *selected* invariants, we were able to obtain the lowest average relative error for all microstructural parameters (Figure 3, bottom right). Considering each individual microstructural parameters, *selected* invariants performs as well as the best individual invariant

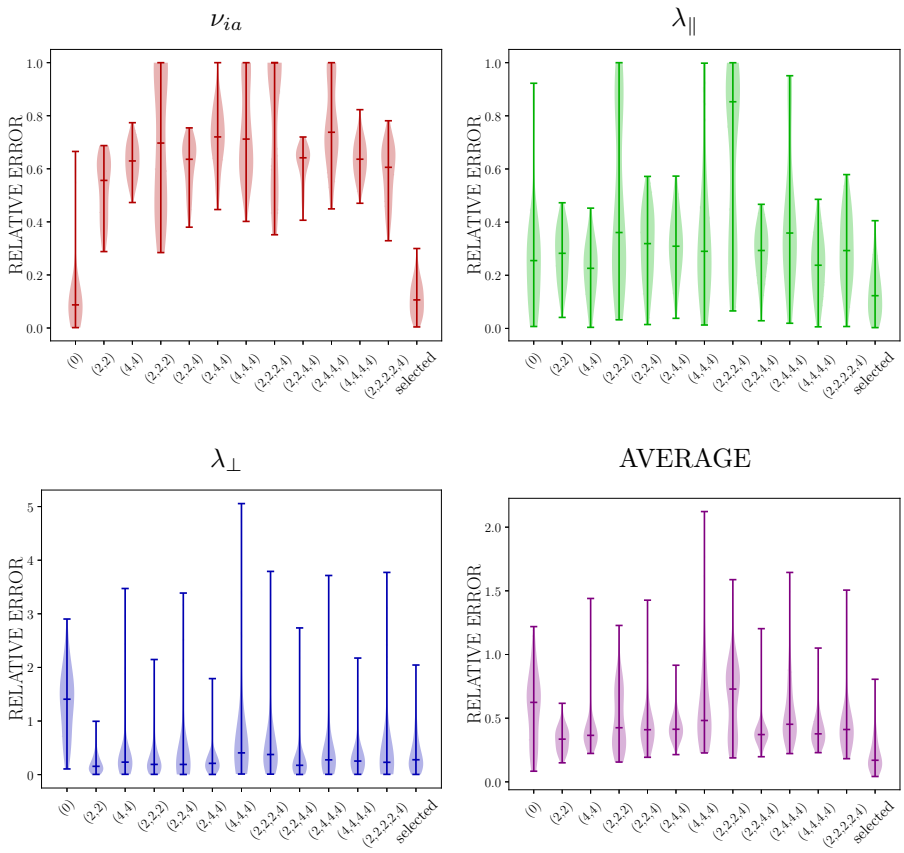

Figure 3: Violin plots for the relative error in the estimation of the microstructural parameters for each individual RIF plus the error for a selected subset of RIF combined together (see main text). Average plot represents the average of the errors over all microstructural parameters.

for what concerns ν_{ia} and $\lambda_{\perp}$, and performs better than any RIF for $\lambda_{\parallel}$. From this synthetic data set analysis, we can infer that all of our RIF are sensitive to tissue microstructure to some degree and combining the best of these we were able to improve the microstructural parameters estimation without changing the signal model or the optimization procedure.

In order to see if these results hold in-vivo we calculate the invariants on the three shells of the diffusion signal of one of the HCP subjects. Figures 4 and 5 show the values of the 12 normalized algebraic independent invariants

on a coronal slice of the subject. The behavior of the invariants appears to be coherent with the results of our first synthetic data. Low-degree invariants $\hat{I}_0[E]$, $\hat{I}_{2,2}[E]$, and $\hat{I}_{2,2,2}[E]$ values seems to decrease with the b-values. High-degree invariants $\hat{I}_{44}[E]$, $\hat{I}_{4,4,4}[E]$, and $\hat{I}_{4,4,4,4}[E]$, on the contrary, are more pronounced at high b-values and seems to be more "noisy" in the lower shells.

In order to investigate the reproducibility of our invariants, we extracted the histogram of the values of the invariants in the CC for each of the subjects. For each histogram, we calculated the Kullback-Leibler divergence (Kullback and Leibler, 1951) between the subjects of the test dataset versus the subjects of the retest dataset (see Supplementary Material Figure 3 to see an example of the resulting divergence matrix). Ideally, every subject of the test dataset should have the lowest divergence with its own brain in the retest dataset. We define the *reproducibility index* for a given invariant as the number of times a test subject shows the lowest divergence for its own retest divided by the number of subjects. Table 3 shows the reproducibility index for all 12 invariants in the three shells and their average. All the invariants show a reproducibility index at least five times above 0.02 which corresponds to the value expected if the lowest divergence was obtained by chance. The lowest reproducible invariant is $\hat{I}_0$ which is basically the mean of the signal. This is probably due to the fact that the mean of the signal is very stable across subjects and it is not specific enough to characterize subject-specif differences. From our analysis, the most reproducible invariant is $\hat{I}_{222}$ which was able to match test and retest for almost half of the subjects for b = 3000 mm^2/s. On average, most of our invariants were able to match at least 30% of the test-retest subjects. The most reproducible shell is the b = 3000 mm^2/s, followed by the b = 2000 mm^2/s, and the b = 1000 mm^2/s. This is not surprising considering that most of our invariants show a higher contrast for bigger b-values.

Figure 6 shows the result of the microstructural parameters fitting for a coronal slice of three HCP subjects. *SMT* rows show the result of the parameters fitting when only a single invariant is considered ($\hat{I}_0[E]$) as in the case of the SMT. *Selected* rows show the result of the fitting when the *selected* invariants

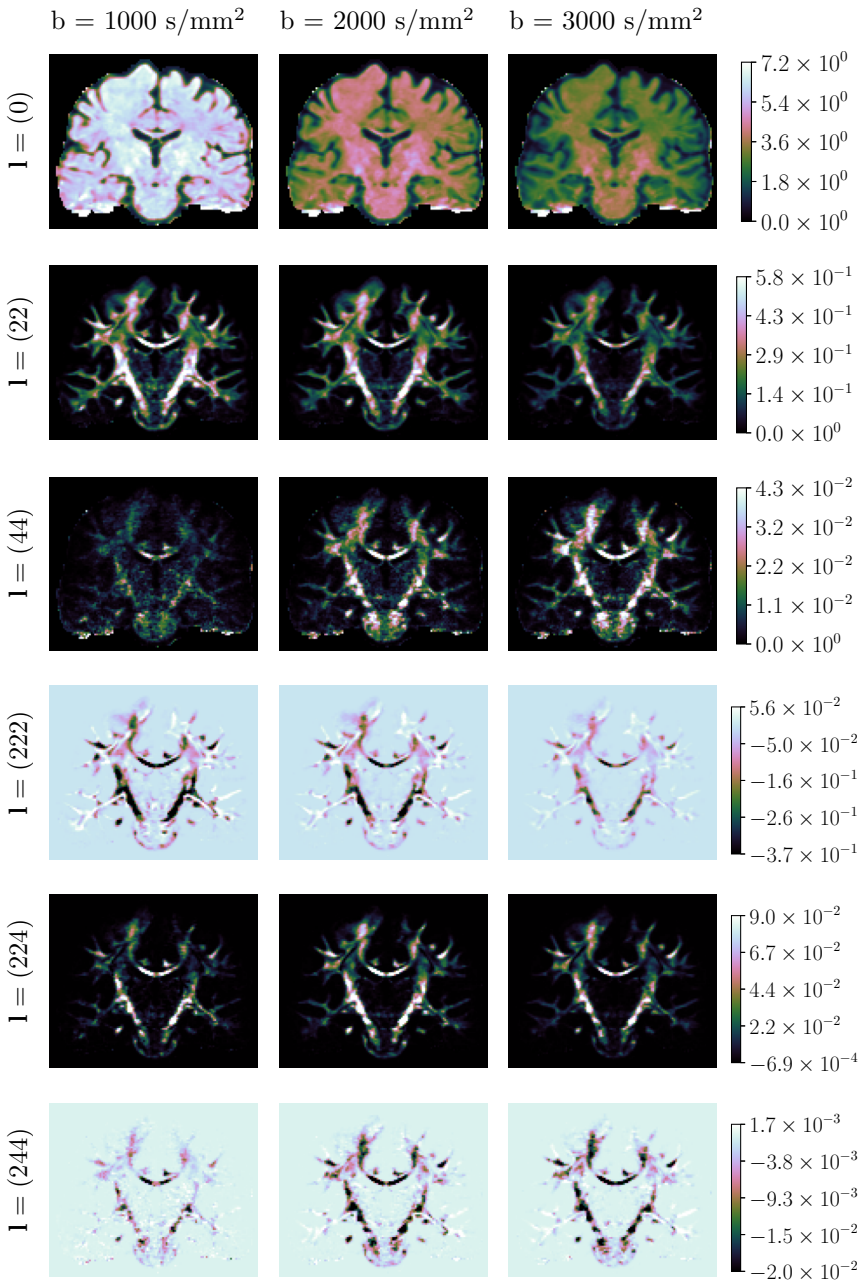

Figure 4: The first six algebraically independent invariants calculated on the diffusion signal of a coronal slice of one of the HCP subjects at different b-values.

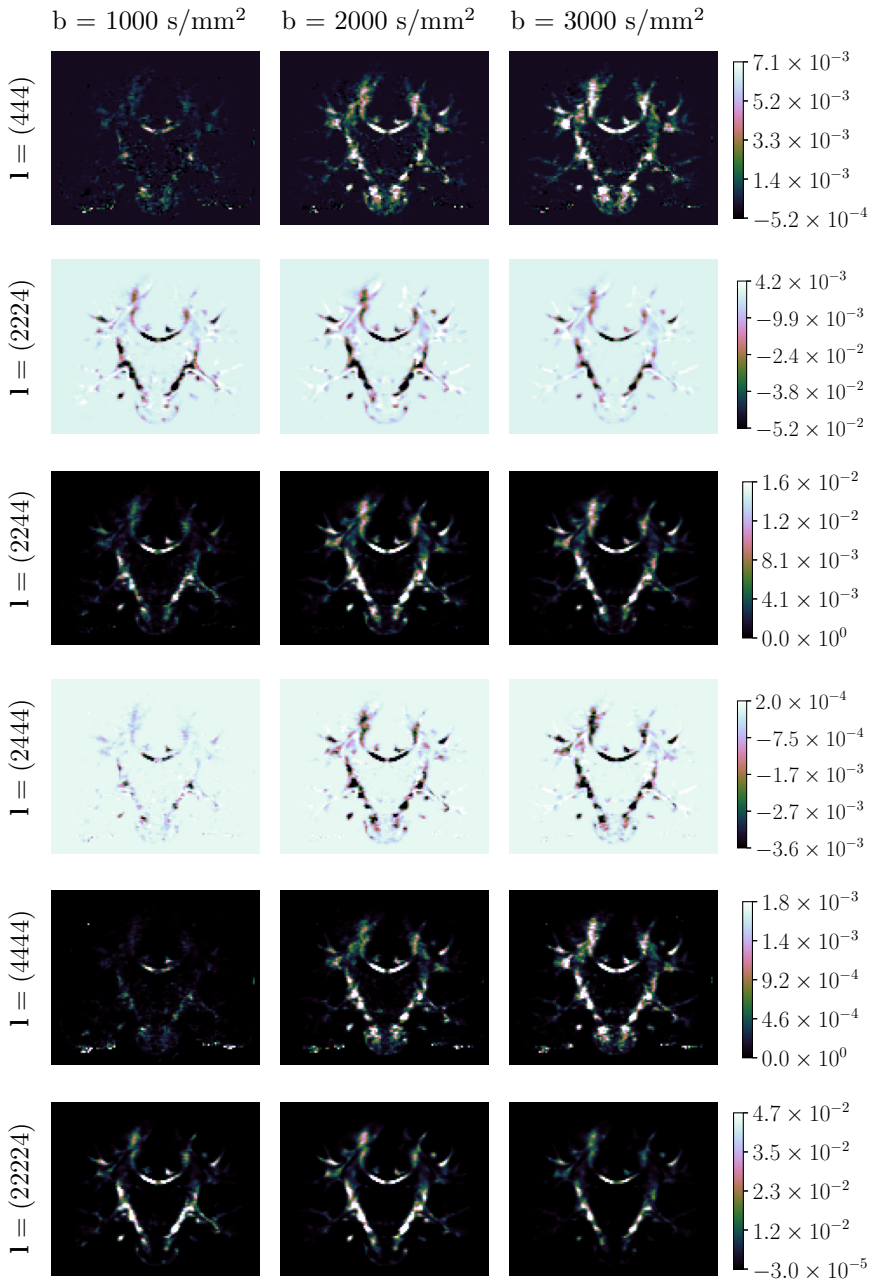

Figure 5: The second six algebraically independent invariants calculated on the diffusion signal of a coronal slice of one of the HCP subjects at different b-values.

	b = 1000 s/mm^2	b = 2000 s/mm^2	b = 3000 s/mm^2	average
$\mathbf{l} = (0)$	0.11	0.18	0.11	0.14
$\mathbf{l} = (22)$	0.32	0.43	0.41	0.39
$\mathbf{l} = (44)$	0.20	0.32	0.27	0.27
$\mathbf{l} = (222)$	0.36	0.43	0.48	0.42
$\mathbf{l} = (224)$	0.27	0.36	0.39	0.34
$\mathbf{l} = (244)$	0.25	0.32	0.36	0.31
$\mathbf{l} = (444)$	0.20	0.25	0.34	0.27
$\mathbf{l} = (2224)$	0.32	0.34	0.45	0.37
$\mathbf{l} = (2244)$	0.23	0.34	0.39	0.32
$\mathbf{l} = (2444)$	0.14	0.36	0.27	0.26
$\mathbf{l} = (4444)$	0.16	0.23	0.25	0.21
$\mathbf{l} = (22224)$	0.25	0.32	0.32	0.30

Table 3: Reproducibility index calculated from the HCP test-retest dataset for all 12 invariants on the three shells and their average.

are considered. For each voxel of the image we run 10 optimizations choosing the starting parameters at random for the initialization. The final image of each of the two techniques represents the median value of the microstructural parameters in the 10 runs.

In all subjects, the SMT fitting presents some black voxels in which the fitting seems to have failed, in particular in the ν_{ia} map. This is probably due to the fact that SMT fitting for more than two microstructural parameters results in an unstable optimization which leads to erroneous parameters values.

On the contrary, the fitting using the *selected* invariants is more stable and results in smoother maps which appear to be more coherent with brain anatomy. In terms of absolute values, ν_{ia} and $\lambda_{\parallel}$ are generally lower in the *selected* invariants maps. In fact, both ν_{ia} and $\lambda_{\parallel}$ reach the respective limit values of 1.0 and 3.0×10^{-3} mm^2/s in most of the white matter voxels when only $\hat{I}_0[E]$ is used for the fitting (Figure 6 top row). For example, in the brainstem, we may

expect a high value of ν_{ia} given the compactness of the fibers going into the corticospinal tracts. However, values of $\nu_{ia} = 1.0$ in the brainstem correspond to not having extra-axonal space at all, which is unlikely in-vivo. It is possible that in the case of the SMT-like fitting, the true minimum of the error function (Eq. (49)) is outside the biophysically plausible range and the optimizer could only push the parameters to the boundaries. On the contrary, using the *selected* set of invariants, the error function is able to find the minimum inside the domain, thanks to the added value of the information provided by the additional invariants. This result also impacts the fitting of $\lambda_\perp$, because in the case of ν_{ia} close to one, there is really no constraint on the parameter estimation of the extra-axonal compartment. The values of $\lambda_\perp$ seem to be higher and smoother for the *selected* invariants with respect to the single invariant fitting. Since we do not know the ground truth values for these features in-vivo we cannot say that the precision of the estimation increased as in the case of the synthetic data set. Therefore, we can speculate that the precision of the maps increases as well, but until in-vivo ground truth values will be known this statement should be taken with cautions, in particular, if the microstructural parameters maps have to be used in a clinical setting.

In order to quantify the changes in the microstructure estimation between the two techniques in-vivo, we calculate the histograms of the three parameters in five ROIs of the CC (Posterior, Mid-Posterior, Central, Mid-Anterior, and Anterior). Figure 7 shows the resulting histograms calculated on the value of each ROIs for the 44 HCP subjects of the test dataset. As can be seen in the figure ν_{ia} and $\lambda_\parallel$ show a bi-modal distribution for CC-Posterior and CC-anterior. On the contrary, the microstructural parameters obtained from the *selected* invariants present a single-mode distributions for ν_{ia} and $\lambda_\parallel$. This is due to the presence of low-value voxels in SMT-derived microstructural maps caused by a failure in the fitting procedure. The values of $\lambda_\perp$ are higher for SMT-fitting with respect to the *selected*-fitting, with wider distribution for this last method. The ground-truth value for $\lambda_\perp$ in the CC is unknown and both distributions seem plausible. Previous works in the literature report a low-high-

low trend for axon diameters in CC from Posterior to Anterior, obtained from both histology (Aboitiz et al., 1992) and dMRI (Alexander et al., 2010). It is interesting to note that the median of the ν_{ia} values from the *selected*-fitting follows a high-low-high trend. Considering that ν_{ia} represents the stick volume-fraction and that low-diameter axons can be modeled as sticks[10], it is plausible that the high stick volume-fractions obtained from our data correspond to a relatively high presence of low diameter axons. The same point can be made for the low stick volume fraction areas corresponding to a higher presence of larger axons. However, these results are still preliminary and to our knowledge, the link between average axons diameter and stick volume-fraction has not been explained in the domain.

6. Discussion

Our work presents a novel framework for analytically calculating RIF from SH representation of spherical functions of any degree. Our results show that we can apply these new invariants to dMRI data showing: i) the relationship between our RIF and classical DTI invariants, ii) the fact that these invariants can be used for tissue microstructural parameters estimation. Moreover, combining a subset of our RIF we were able to improve the microstructural feature estimation without changing the underneath microstructural model as done in Zucchelli et al. (2018a).

In dMRI literature, several authors have tried to compute all the algebraically independent invariants from a set of SH coefficients of a given maximum SH degree. Ghosh et al. (2012b) and Papadopoulo et al. (2014) proposed a technique, specific for the 4^{th} rank tensor, recovering all 12 algebraically independent invariants. The Caruyer and Verma (2015) framework, given any SH degree, was able to obtain all the algebraically independent RIF. Such a

[10]The accuracy of the stick model for small-diameter axons (e.g $\leq 3\ \mu m$) depends on the gradient strength, pulse width, and the pulse separation time of the diffusion acquisition. For what concern the HCP protocol the stick is indeed a valid model for small axons.

framework considers all the polynomials invariant to a rotation of 1 degree with respect to the x and z axes, which the authors proved to be rotation invariant to any further rotation. The number of RIF generated with this technique is extremely high, in fact, more than 30000 RIF are created for a SH degree of $L = 6$. The biggest limitation of this framework is that the generated invariants cannot be expressed under a general closed-form. In fact, in the work of Caruyer and Verma (2015), each of the invariants has a unique and non-trivial expression. Gaunt coefficients have already been used in dMRI for generating RIF in the work of Schwab et al. (2013). Their invariant framework is based on the calculation of the eigenvalues of a Gaunt coefficients matrix. As in the case of Caruyer and Verma (2015), the main limitation of the Schwab et al. (2013) framework is the absence of a closed-form formula for the invariants. Moreover, there are no guarantees that the Schwab et al. (2013) method generates a complete set of algebraically independent RIF. The main advantage of our framework over the state of the art is that, thanks to Eq. (21), we are able to generate RIF from the SH representation of any spherical functions of any degree *analytically*. Only a few of these RIF will be non-zero and it is easy to verify which of them form an algebraically independent set.

Rotation invariants are a subject of interest in several research fields including pattern recognition and computer vision (Kakarala and Mao, 2010; Kondor, 2007). We believe that our framework will be interesting for many non-diffusion applications. The compactness of our mathematical formulation makes the implementation and the extension of the invariants extremely simple even for large SH degree compared to similar techniques presented in the state of the arts.

For what concerns the poor performances of SMT on the HCP data with respect to previously reported results (Kaden et al., 2016a) this is probably related to the fact that we have three microstructural parameters to be fitted with respect to the two parameters fitting used in most of the SMT publications (Zucchelli et al., 2018a). Recent works (Novikov et al., 2018b; Reisert et al., 2016) have highlighted the importance of the use of RIF in dMRI for estimating tissue microstructural properties. Our results confirm that our additional RIF improve

the estimation of brain microstructure. We need to stress that one of our goals was to show that our RIF can improve the estimation of microstructural parameters in dMRI, independently of the considered microstructural model. The degeneracy of the microstructural parameter estimation is still an open problem in dMRI (Jelescu et al., 2016; Novikov et al., 2018a; Coelho et al., 2018) and our new RIF can be considered a useful tool for aiding solving it. Although the microstructural model used in this work was simpler than NODDIDA (Jelescu et al., 2016) or the standard model (Novikov et al., 2016) we believe that any model could benefit from our invariants.

Some important questions concerning the invariants remain open. For example, in our study, we consider SH only up to degree $L = 4$. It is possible that adding more invariants, at a higher degree, will provide even a more precise estimation of the microstructural parameters, especially in the high b-values shells. In fact, it may be possible that 12 RIF are too many for the b=1000 s/mm^2 shell and too few for the b=3000 s/mm^2 shell. Identifying the optimal number of invariants for experiments with different b-values could be a topic of interesting work for the future as well as testing our RIF with more complex microstructural models.

7. Conclusion

In this work, we provided an analytical framework for generating rotation invariants functions from spherical signals. These new RIF are the natural expansion of power-spectrum and bispectrum invariants and are deeply linked to statistical and geometrical measures of spherical functions. We applied our new RIF to dMRI data in two fashions. First to the ADC in order to verify the link between our RIF and the existing dMRI invariants. Secondly, we calculated the invariants on the fODF and the diffusion signal itself, verifying that our RIF are reproducible and can improve the estimation of the brain tissue microstructure. This first practical application will be the cornerstone of our future research where we will investigate the possibility of exploiting the invari-

ants for applications such as *image registration*, *data harmonization*, and *brain surface modeling*.

8. Acknowledgments

This work has received funding from the European Research Council (ERC) under the European Union's Horizon 2020 research and innovation program (ERC Advanced Grant agreement No 694665 : CoBCoM - Computational Brain Connectivity Mapping).

Data were provided by the Human Connectome Project, WU-Minn Consortium (Principal Investigators: David Van Essen and Kamil Ugurbil; 1U54MH091657) funded by the 16 NIH Institutes and Centers that support the NIH Blueprint for Neuroscience Research; and by the McDonnell Center for Systems Neuroscience at Washington University.

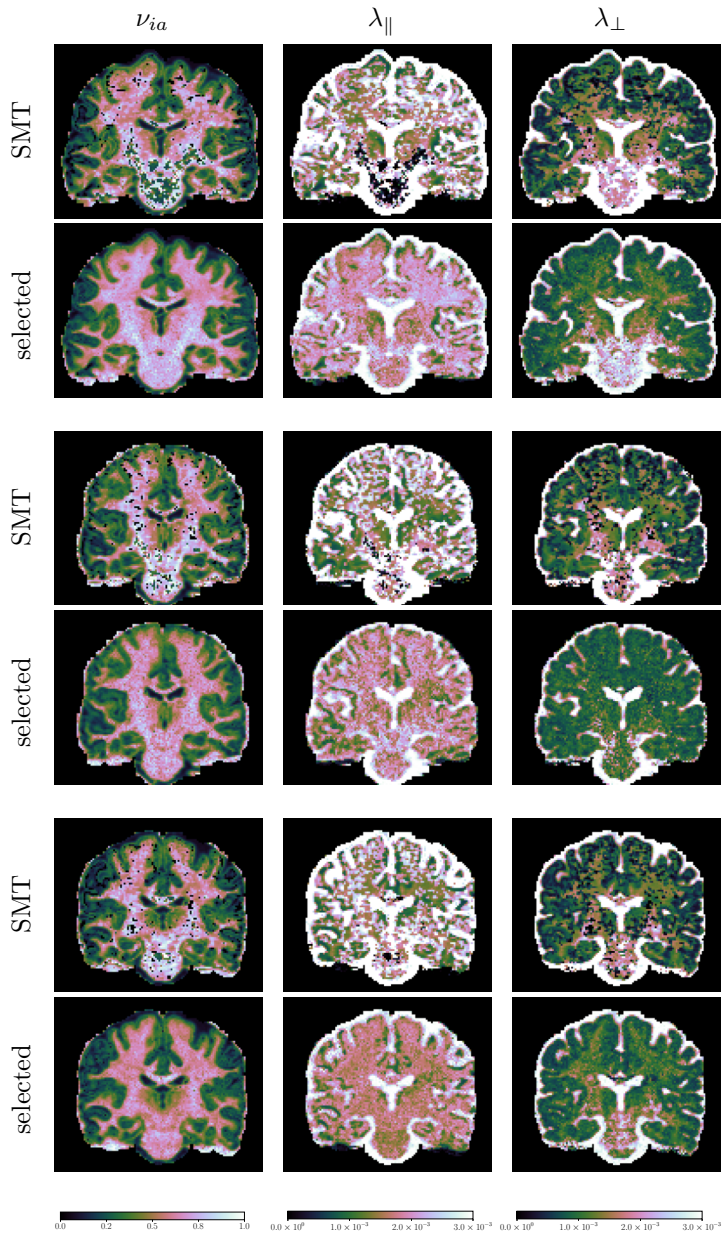

Figure 6: Microstructural parameter estimation comparison between a single invariant fitting (*SMT* rows) and the fitting performed including the selected invariants whose achieved the best performances on the synthetic data set (*selected* rows) on a coronal slice of three of the HCP subjects (160123, 174437, 473952).

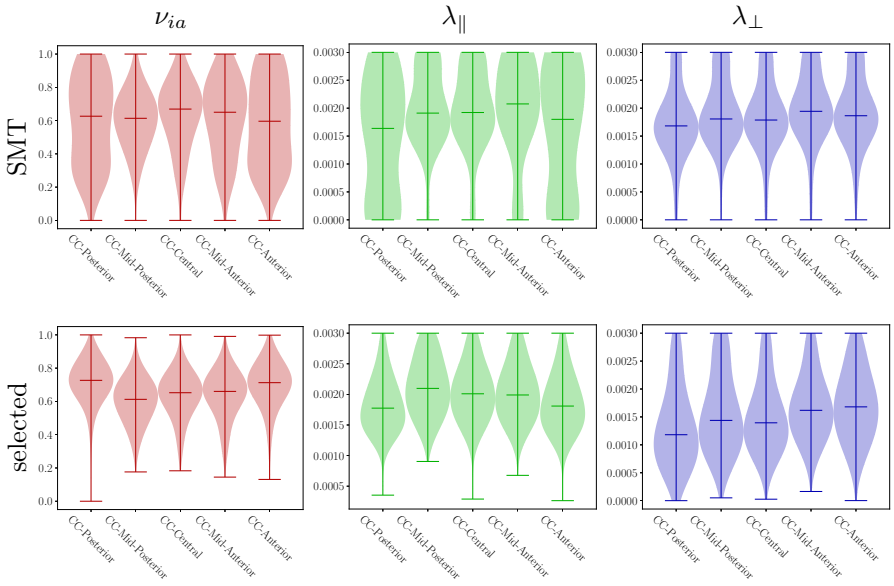

Figure 7: Violin plots calculated on the microstructural parameters on 5 ROIs of the Corpus Callosum (CC) for 44 HCP subjects. Top row correspond to a single invariant fitting (SMT) and bottom row the fitting performed including the selected invariants (*selected*).

Appendix A. The generalized invariants are RIF

$I_{\mathbf{l}}[f]$ is rotation invariant feature iff $I_{\mathbf{l}}[f] = I_{\mathbf{l}}[Rf] = I_{\mathbf{l}}[h]$. Given the rotated SH series expansion $h(\mathbf{u})$ we can show that

$$\begin{aligned}
I_{l_1 \dots l_d}[h] &= \int_{S^2} \prod_{i=1}^{d} \left[\sum_{m_i'=-l_i}^{l_i} g_{l_i m_i'} Y_{l_i}^{m_i'}(\mathbf{u}) \right] d\mathbf{u} \\
&= \int_{S^2} \prod_{i=1}^{d} \left[\sum_{m_i'=-l_i}^{l_i} \sum_{m_i=-l_i}^{l_i} c_{l_i m_i} D_{m_i', m_i}^{l_i}(R) Y_{l_i}^{m_i'}(\mathbf{u}) \right] d\mathbf{u} \\
&= \int_{S^2} \prod_{i=1}^{d} \left[\sum_{m_i=-l_i}^{l_i} c_{l_i m_i} \sum_{m_i'=-l_i}^{l_i} D_{m_i', m_i}^{l_i}(R) Y_{l_i}^{m_i'}(\mathbf{u}) \right] d\mathbf{u} \\
&= \int_{S^2} \prod_{i=1}^{d} \left[\sum_{m_i=-l_i}^{l_i} c_{l_i m_i} Y_l^m(R^{-1}\mathbf{u}) \right] d\mathbf{u} \\
&= \int_{S^2} \sum_{m_1=-l_1}^{l_1} \cdots \sum_{m_d=-l_d}^{l_d} c_{l_1 m_1} \cdots c_{l_d m_d} Y_{l_1}^{m_1}(R^{-1}\mathbf{u}) \cdots Y_{l_d}^{m_d}(R^{-1}\mathbf{u}) d\mathbf{u} \\
&= \sum_{m_1=-l_1}^{l_1} \cdots \sum_{m_d=-l_d}^{l_d} c_{l_1 m_1} \cdots c_{l_d m_d} \int_{S^2} Y_{l_1}^{m_1}(R^{-1}\mathbf{u}) \cdots Y_{l_d}^{m_d}(R^{-1}\mathbf{u}) d\mathbf{u} \\
&= \sum_{m_1=-l_1}^{l_1} \cdots \sum_{m_d=-l_d}^{l_d} c_{l_1 m_1} \cdots c_{l_d m_d} G(l_1, m_1 | \cdots | l_d, m_d) \\
&= I_{l_1 \dots l_d}^{d}[f]
\end{aligned} \tag{A.1}$$

which proves that $I_{\mathbf{l}}[f] = I_{\mathbf{l}}[Rf]$.

References

Aboitiz, F., Scheibel, A. B., Fisher, R. S., Zaidel, E., 1992. Fiber composition of the human corpus callosum. Brain research 598 (1), 143–153.

Alexander, D. C., Hubbard, P. L., Hall, M. G., Moore, E. A., Ptito, M., Parker, G. J., Dyrby, T. B., 2010. Orientationally invariant indices of axon diameter and density from diffusion MRI. NeuroImage 52 (4), 1374 – 1389.

Anderson, A. W., 2005. Measurement of fiber orientation distributions using high angular resolution diffusion imaging. Magnetic Resonance in Medicine 54 (5), 1194–1206.

Assaf, Y., Blumenfeld-Katzir, T., Yovel, Y., Basser, P. J., 2008. Axcaliber: a method for measuring axon diameter distribution from diffusion mri. Magnetic Resonance in Medicine 59 (6), 1347–1354.

Basser, P. J., Mattiello, J., LeBihan, D., 1994. MR diffusion tensor spectroscopy and imaging. Biophys J 66 (1), 259.

Baxansky, A., Kiryati, N., 2007. Calculating geometric properties of three-dimensional objects from the spherical harmonic representation. Pattern Recognition 40 (2), 756 – 770.
URL http://www.sciencedirect.com/science/article/pii/S003132030600272X

Caruyer, E., Lenglet, C., Sapiro, G., Deriche, R., 2013. Design of multishell sampling schemes with uniform coverage in diffusion mri. Magnetic resonance in medicine 69 (6), 1534–1540.

Caruyer, E., Verma, R., 2015. On facilitating the use of hardi in population studies by creating rotation-invariant markers. Medical image analysis 20 (1), 87–96.

Coelho, S., Pozo, J. M., Jespersen, S. N., Jones, D. K., Frangi, A. F., 2018. Double diffusion encoding prevents degeneracy in parameter estimation of biophysical models in diffusion mri. arXiv preprint arXiv:1809.05059.

Descoteaux, M., Angelino, E., Fitzgibbons, S., Deriche, R., 2007. Regularized, fast, and robust analytical q-ball imaging. Magnetic Resonance in Medicine 58 (3), 497–510.

Edén, M., 2003. Computer simulations in solid-state nmr. iii. powder averaging. Concepts in Magnetic Resonance Part A: An Educational Journal 18 (1), 24–55.

Ehrenborg, R., Rota, G.-C., 1993. Apolarity and canonical forms for homogeneous polynomials. European Journal of Combinatorics 14 (3), 157–181.

Fischl, B., Salat, D. H., Busa, E., Albert, M., Dieterich, M., Haselgrove, C., van der Kouwe, A., Killiany, R., Kennedy, D., Klaveness, S., Montillo, A., Makris, N., Rosen, B., Dale, A. M., 2002. Whole brain segmentation: automated labeling of neuroanatomical structures in the human brain. Neuron 33, 341–355.

Frank, L. R., 2002. Characterization of anisotropy in high angular resolution diffusion-weighted mri. Magnetic Resonance in Medicine 47 (6), 1083–1099. URL https://onlinelibrary.wiley.com/doi/abs/10.1002/mrm.10156

Ghosh, A., Papadopoulo, T., Deriche, R., May 2012a. Biomarkers for hardi: 2nd amp; 4th order tensor invariants. In: 2012 9th IEEE International Symposium on Biomedical Imaging (ISBI). pp. 26–29.

Ghosh, A., Papadopoulo, T., Deriche, R., 2012b. Generalized invariants of a 4th order tensor: Building blocks for new biomarkers in dmri. In: Proceedings of the Computation Diffusion MRI Workshop at the MICCAI Conference.

Homeier, H. H., Steinborn, E., 1996. Some properties of the coupling coefficients of real spherical harmonics and their relation to gaunt coefficients. Journal of Molecular Structure: THEOCHEM 368, 31 – 37, proceedings of the Second Electronic Computational Chemistry Conference.

Jelescu, I. O., Veraart, J., Fieremans, E., Novikov, D. S., 2016. Degeneracy in model parameter estimation for multi-compartmental diffusion in neuronal tissue. NMR in Biomedicine 29 (1), 33–47, nBM-15-0204.R2.

Jespersen, S. N., Bjarkam, C. R., Nyengaard, J. R., Chakravarty, M. M., Hansen, B., Vosegaard, T., stergaard, L., Yablonskiy, D., Nielsen, N. C., Vestergaard-Poulsen, P., 2010. Neurite density from magnetic resonance diffusion measurements at ultrahigh field: Comparison with light microscopy and electron microscopy. NeuroImage 49 (1), 205 – 216.

Jespersen, S. N., Kroenke, C. D., stergaard, L., Ackerman, J. J., Yablonskiy, D. A., 2007. Modeling dendrite density from magnetic resonance diffusion measurements. NeuroImage 34 (4), 1473 – 1486.

Kaden, E., Kelm, N. D., Carson, R. P., Does, M. D., Alexander, D. C., 2016a. Multi-compartment microscopic diffusion imaging. NeuroImage 139, 346 – 359.

Kaden, E., Kruggel, F., Alexander, D. C., 2016b. Quantitative mapping of the per-axon diffusion coefficients in brain white matter. Magnetic Resonance in Medicine 75 (4), 1752–1763.

Kakarala, R., Mao, D., June 2010. A theory of phase-sensitive rotation invariance with spherical harmonic and moment-based representations. In: 2010 IEEE Computer Society Conference on Computer Vision and Pattern Recognition. pp. 105–112.

Kayal, N., July 2009. The complexity of the annihilating polynomial. In: 2009 24th Annual IEEE Conference on Computational Complexity. pp. 184–193.

Kondor, R., 2007. A novel set of rotationally and translationally invariant features for images based on the non-commutative bispectrum. arXiv preprint cs/0701127.

Kullback, S., Leibler, R. A., 03 1951. On information and sufficiency. Ann. Math. Statist. 22 (1), 79–86.

Lampinen, B., Szczepankiewicz, F., Mrtensson, J., van Westen, D., Sundgren, P. C., Nilsson, M., 2017. Neurite density imaging versus imaging of microscopic anisotropy in diffusion mri: A model comparison using spherical tensor encoding. NeuroImage 147, 517 – 531.
URL http://www.sciencedirect.com/science/article/pii/S105381191630670X

McKinnon, E. T., Jensen, J. H., Glenn, G. R., Helpern, J. A., 2017. Dependence on b-value of the direction-averaged diffusion-weighted imaging signal in brain. Magnetic resonance imaging 36, 121–127.

Novikov, D. S., Jespersen, S. N., Kiselev, V. G., Fieremans, E., 2016. Quantifying brain microstructure with diffusion mri: Theory and parameter estimation. arXiv preprint arXiv:1612.02059.

Novikov, D. S., Veraart, J., Jelescu, I. O., Fieremans, E., 2018a. Rotationally-invariant mapping of scalar and orientational metrics of neuronal microstructure with diffusion mri. NeuroImage 174, 518 – 538.
URL http://www.sciencedirect.com/science/article/pii/S1053811918301915

Novikov, D. S., Veraart, J., Jelescu, I. O., Fieremans, E., 2018b. Rotationally-invariant mapping of scalar and orientational metrics of neuronal microstructure with diffusion mri. NeuroImage 174, 518 – 538.

Özarslan, E., Koay, C. G., Shepherd, T. M., Komlosh, M. E., İrfanoğlu, M. O., Pierpaoli, C., Basser, P. J., 2013. Mean apparent propagator (map) mri: a novel diffusion imaging method for mapping tissue microstructure. NeuroImage 78, 16–32.

Özarslan, E., Mareci, T. H., 2003. Generalized diffusion tensor imaging and analytical relationships between diffusion tensor imaging and high angular resolution diffusion imaging. Magnetic Resonance in Medicine 50 (5), 955–965.
URL https://onlinelibrary.wiley.com/doi/abs/10.1002/mrm.10596

Özarslan, E., Vemuri, B. C., Mareci, T. H., 2005. Generalized scalar measures for diffusion mri using trace, variance, and entropy. Magnetic Resonance in Medicine 53 (4), 866–876.
URL https://onlinelibrary.wiley.com/doi/abs/10.1002/mrm.20411

Papadopoulo, T., Ghosh, A., Deriche, R., 2014. Complete set of invariants of a 4th order tensor: The 12 tasks of hardi from ternary quartics. In: Golland, P., Hata, N., Barillot, C., Hornegger, J., Howe, R. (Eds.), Medical Image Computing and Computer-Assisted Intervention – MICCAI 2014. Springer International Publishing, Cham, pp. 233–240.

Reisert, M., Kellner, E., Dhital, B., Hennig, J., Kiselev, V. G., 2016. Disentangling micro from mesostructure by diffusion mri: A bayesian approach. NeuroImage, –.

Santis, S. D., Gabrielli, A., Palombo, M., Maraviglia, B., Capuani, S., 2011. Non-gaussian diffusion imaging: a brief practical review. Magnetic Resonance Imaging 29 (10), 1410 – 1416, proceedings of the International School on Magnetic Resonance and Brain Function.

Schultz, T., Fuster, A., Ghosh, A., Deriche, R., Florack, L., Lim, L.-H., 2014. Higher-order tensors in diffusion imaging. In: Westin, C.-F., Vilanova, A., Burgeth, B. (Eds.), Visualization and Processing of Tensors and Higher Order Descriptors for Multi-Valued Data. Springer Berlin Heidelberg, Berlin, Heidelberg, pp. 129–161.

Schwab, E., Çetingül, H. E., Afsari, B., Yassa, M. A., Vidal, R., 2013. Rotation invariant features for hardi. In: Gee, J. C., Joshi, S., Pohl, K. M., Wells, W. M., Zöllei, L. (Eds.), Information Processing in Medical Imaging. Springer Berlin Heidelberg, Berlin, Heidelberg, pp. 705–717.

Schwartz, J. T., Oct. 1980. Fast probabilistic algorithms for verification of polynomial identities. J. ACM 27 (4), 701–717.

Sotiropoulos, S. N., Jbabdi, S., Xu, J., Andersson, J. L., Moeller, S., Auerbach, E. J., Glasser, M. F., Hernandez, M., Sapiro, G., Jenkinson, M., et al., 2013. Advances in diffusion MRI acquisition and processing in the human connectome project. Neuroimage 80, 125–143.

Tournier, J.-D., Calamante, F., Connelly, A., 2007. Robust determination of the fibre orientation distribution in diffusion mri: non-negativity constrained super-resolved spherical deconvolution. NeuroImage 35 (4), 1459–1472.

Tournier, J.-D., Calamante, F., Gadian, D. G., Connelly, A., 2004. Direct estimation of the fiber orientation density function from diffusion-weighted mri data using spherical deconvolution. NeuroImage 23 (3), 1176–1185.

Zhang, H., T., S., Wheeler-Kingshott, C., Alexander, D., 2012. NODDI: Practical in vivo neurite orientation dispersion and density imaging of the human brain. Neuroimage 61 (4), 1000–1016.

Zippel, R., 1979. Probabilistic algorithms for sparse polynomials. In: Ng, E. W. (Ed.), Symbolic and Algebraic Computation. Springer Berlin Heidelberg, Berlin, Heidelberg, pp. 216–226.

Zucchelli, M., Descoteaux, M., Menegaz, G., 2017. Noddi-sh: a computational efficient noddi extension for fodf estimation in diffusion mri. arXiv preprint arXiv:1708.08999.

Zucchelli, M., Descoteaux, M., Menegaz, G., 2018a. A generalized smt-based framework for diffusion mri microstructural model estimation. In: Computational Diffusion MRI. Springer, pp. 51–63.

Zucchelli, M., Deslauriers-Gauthier, S., Deriche, R., Sep. 2018b. A Closed-Form Solution of Rotation Invariant Spherical Harmonic Features in Diffusion MRI. In: MICCAI - Computational Diffusion MRI Workshop 2018. Granada, Spain. URL `https://hal.inria.fr/hal-01912148`

Supplementary Material: A Computational Framework For Generating Rotation Invariant Features And Its Application In Diffusion MRI

1 SH definition and properties

The complex Spherical Harmonics (SH) $y_l^m(\mathbf{u})$ are defined as

$$y_l^m(\theta,\phi) = i^{m+|m|}\sqrt{\frac{(2l+1)(l-|m|)!}{4\pi(l+|m|)!}}P_l^{|m|}(\cos\theta)\exp(im\phi). \tag{1}$$

The real SH can be calculated as

$$Y_l^m = \begin{cases} \sqrt{2}\cdot Re(y_l^{|m|}), & \text{if } m>0 \\ Re(y_l^0), & \text{if } m=0 \\ \sqrt{2}\cdot Img(y_l^{|m|}), & \text{if } m<0 \end{cases} \tag{2}$$

For real SH the following equations holds:

$$Y_0^0 = \frac{1}{\sqrt{4\pi}} \tag{3}$$

$$Y_2^{-2} = \sqrt{\frac{15}{16\pi}}\sin(\theta)^2\sin(2\phi) \tag{4}$$

$$Y_2^{-1} = -\sqrt{\frac{15}{4\pi}}\sin(\theta)\cos(\theta)\sin(\phi) \tag{5}$$

$$Y_2^0 = \sqrt{\frac{5}{16\pi}}\left(3\cos(\theta)^2-1\right) \tag{6}$$

$$Y_2^1 = -\sqrt{\frac{15}{4\pi}}\sin(\theta)\cos(\theta)\cos(\phi) \tag{7}$$

$$Y_2^2 = \sqrt{\frac{15}{16\pi}}\sin(\theta)^2\cos(2\phi) \tag{8}$$

$$\sum_{m=-l}^{l}(Y_l^m)^2 = \frac{2l+1}{4\pi} \tag{9}$$

$$\sum_{m=-l}^{l}Y_l^m(\mathbf{u})Y_l^m(\mathbf{v}) = \frac{2l+1}{4\pi}P_l(\mathbf{u}\cdot\mathbf{v}) \tag{10}$$

$$\int_{S^2}Y_l^m(\mathbf{u})d\mathbf{u} = \sqrt{4\pi}\delta_{lm}^{00} \tag{11}$$

$$\int_{S^2}Y_l^m(\mathbf{u})Y_{l'}^{m'}(\mathbf{u})d\mathbf{u} = \delta_{lm}^{l'm'} \tag{12}$$

$$\int_{S^2}Y_{l_1}^{m_1}(\mathbf{u})Y_{l_2}^{m_2}(\mathbf{u})Y_{l_3}^{m_3}(\mathbf{u})d\mathbf{u} = G(l_1,m_1|l_2,m_2|l_3,m_3) \tag{13}$$

2 Funk-Hecke Theorem

The **Funk-Hecke Theorem** (Descoteaux et al., 2007) states that:

Theorem. *Let $f(t)$ be continuous on $[-1,1]$ and H_l any SH of degree l in C^3, the space of 3D complex functions. Then, given a unit vector $\vec{\boldsymbol{u}}$*

$$\int_{|\vec{\boldsymbol{v}}|=1} f(\vec{\boldsymbol{u}}^T\vec{\boldsymbol{v}})H_l(\vec{\boldsymbol{v}})d\vec{\boldsymbol{v}} = \alpha_l H_l(\vec{\boldsymbol{u}}) \tag{14}$$

where α_l is defined as

$$\alpha_l = 2\pi\int_{-1}^{1} P_l(t)f(t)dt \tag{15}$$

with P_l the Legendre polynomial of degree l.

3 The Dirac's delta function has maximum fODF invariants

We are interested in searching for the maximum value of our new invariants when calculated on the fiber Orientation Distribution Function (fODF) $\rho(\boldsymbol{u})$. The fODF presents some interesting properties: its symmetric, always non-negative, and its integral is one. In dMRI literature, the fODF has been often represented as a Watson distribution (Zhang et al. 2012)

$$W(\kappa,\boldsymbol{v},\boldsymbol{u}) = \frac{1}{4\pi_1F_1(1/2,3/2,\kappa)}\exp(\kappa\ \boldsymbol{v}\cdot\boldsymbol{u}) \tag{16}$$

where $\boldsymbol{v}$ is the unit vector representing the distribution main direction and κ is the concentration parameter of the distribution.

$$\begin{aligned} c_{lm}(k,\boldsymbol{v}) &= \int_{S^2} W(\kappa,\boldsymbol{v},\boldsymbol{u})Y_l^m(\boldsymbol{u})d\boldsymbol{u} \\ &= \frac{1}{2\ {}_1F_1(1/2,3/2,\kappa)}\kappa^{l/2}\frac{\Gamma(l/2+1/2)}{\Gamma(l+3/2)}\ {}_1F_1(l+1/2,l/2+3/2,\kappa)Y_l^m(\boldsymbol{v}) \end{aligned} \tag{17}$$

The limit of the Watson SH coefficients for increasing κ is

$$\lim_{\kappa\to\infty} c_{lm}(k,\boldsymbol{v}) = Y_l^m(\boldsymbol{v}) \tag{18}$$

which corresponds to the SH coefficients of the Dirac delta function. In fact:

$$\begin{aligned} c_{lm}(\boldsymbol{v}) &= \int_{S^2}\delta(\boldsymbol{v},\boldsymbol{u})Y_l^m(\boldsymbol{u})d\boldsymbol{u} \\ &= Y_l^m(\boldsymbol{v}) \end{aligned} \tag{19}$$

where $\delta(\boldsymbol{v},\boldsymbol{u})$ is the Dirac delta pointing in the direction of $\boldsymbol{v}$. Since a completely dispersed isotropic fODF presents the lowest absolute values for the invariants we may guess that highly concentrated fODF have higher invariants and the maximum invariants could be reached for the limit value of the concentration: the Dirac's delta function. In fact, as it possible to see from Figure **??** *the normalized invariants tend to reach the value of the Dirac's delta invariants as the concentration parameter κ increases.*

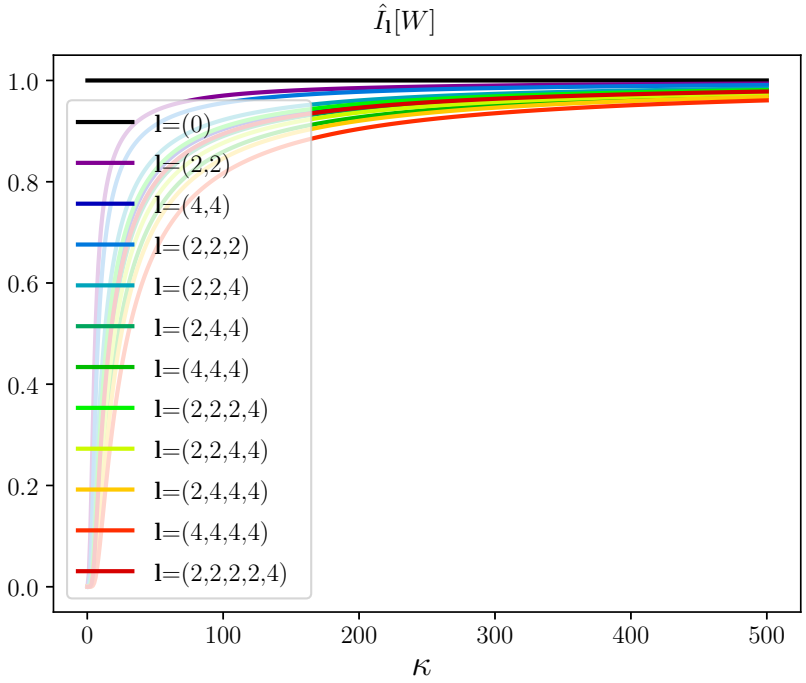

Figure 1: The normalized invariants for the Watson distribution as the concentration parameter κ increases.

One of the main limitations of the use of Watson distribution for representing the fODF is the fact that the Watson is a unimodal distribution and cannot represent crossing fibers. However, we can easily tackle this problem considering the sum of two Watson distributions. E.g. we can consider the fODF as

$$\rho(\kappa, \boldsymbol{v}_1, \boldsymbol{v}_2, \boldsymbol{u}) = \frac{1}{2}W(\kappa, \boldsymbol{v}_1, \boldsymbol{u}) + \frac{1}{2}W(\kappa, \boldsymbol{v}_2, \boldsymbol{u}) \tag{20}$$

If we consider the normalized invariants as a function of the crossing angle $\boldsymbol{v}_1 \cdot \boldsymbol{v}_2$ we expect the highest value to correspond to perfectly aligned Watson distributions, namely when $\boldsymbol{v}_1 \cdot \boldsymbol{v}_2 = 1$ or $\boldsymbol{v}_1 \cdot \boldsymbol{v}_2 = -1$. This because the higher the crossing angle between the two distributions the more dispersed our fODF will be. Figure **??** *shows exactly this behavior for different values of κ. As in the case of the single Watson distribution, higher κ corresponds to higher invariants and, as expected, lower crossing angles increase the value of the invariants.*

Although these results do not prove that the Dirac delta function invariants have maximum value with respect to any other spherical functions, it is safe to assume that the Dirac delta invariants are the maximum while considering the restricted space of the functions representing fODF, at least for the 12 rotation invariant features considered in this work.

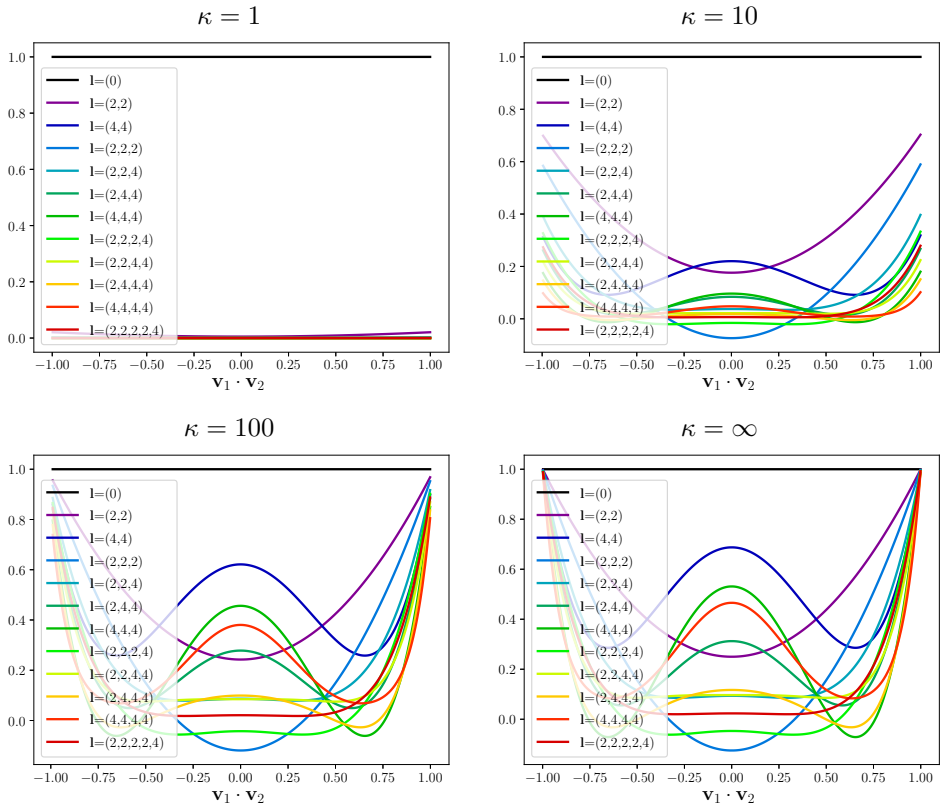

Figure 2: The normalized invariants for the fODF generated using the sum of two Watson distributions aligned in the directions $\mathbf{v}_1$ and $\mathbf{v}_2$ respectively, for different concentration parameters κ.

4 Calculation of DTI invariants

DTI invariant $I_{22}[D]$ can be calculated as

$$
\begin{aligned}
I_{22}[D] &= \sum_{m=-2}^{2} [c_{2m}]^2 \\
&= \sum_{m=-2}^{2} \left[\frac{8\pi}{15} \sum_{i=1}^{3} \lambda_i Y_2^m(\boldsymbol{v}_i) \right]^2 \\
&= \left(\frac{8\pi}{15} \right)^2 \sum_{m=-2}^{2} \left[\sum_{i=1}^{3} \lambda_i Y_2^m(\boldsymbol{v}_i) \right]^2 \\
&= \frac{64\pi^2}{225} \sum_{m=-2}^{2} \left[\sum_{i=1}^{3} \lambda_i Y_2^m(\boldsymbol{v}_i) \right]^2 \\
&= \frac{64\pi^2}{225} \sum_{m=-2}^{2} [\lambda_1 Y_2^m(\boldsymbol{v}_1)]^2 + [\lambda_2 Y_2^m(\boldsymbol{v}_2)]^2 + [\lambda_3 Y_2^m(\boldsymbol{v}_3)]^2 + \\
&+ 2\lambda_1\lambda_2 Y_2^m(\boldsymbol{v}_1) Y_2^m(\boldsymbol{v}_2) + 2\lambda_2\lambda_3 Y_2^m(\boldsymbol{v}_2) Y_2^m(\boldsymbol{v}_3) + 2\lambda_1\lambda_3 Y_2^m(\boldsymbol{v}_1) Y_2^m(\boldsymbol{v}_3) \\
&= \frac{64\pi^2}{225} \left[\lambda_1^2 \left(\frac{5}{4\pi} \right) + \lambda_2^2 \left(\frac{5}{4\pi} \right) + \lambda_3^2 \left(\frac{5}{4\pi} \right) + 2\lambda_1\lambda_2 \left(\frac{5}{4\pi} \right) P_2(\boldsymbol{v}_1 \boldsymbol{v}_2) + \right. \\
&\left. + 2\lambda_2\lambda_3 \left(\frac{5}{4\pi} \right) P_2(\boldsymbol{v}_2 \boldsymbol{v}_3) + 2\lambda_1\lambda_3 \left(\frac{5}{4\pi} \right) P_2(\boldsymbol{v}_1 \boldsymbol{v}_3) \right] \\
&= \frac{64\pi^2}{225} \frac{5}{4\pi} \left[\lambda_1^2 + \lambda_2^2 + \lambda_3^2 - \lambda_1\lambda_2 - \lambda_2\lambda_3 - \lambda_1\lambda_3 \right] \\
&= \frac{16\pi}{45} \left[\lambda_1^2 + \lambda_2^2 + \lambda_3^2 - \lambda_1\lambda_2 - \lambda_2\lambda_3 - \lambda_1\lambda_3 \right] \\
&= \frac{8\pi}{45} \left[(\lambda_1 - \lambda_2)^2 + (\lambda_1 - \lambda_3)^2 + (\lambda_2 - \lambda_3)^2 \right]
\end{aligned}
\tag{21}
$$

exploiting Eq. (??), Eq. (??) and the fact that $P_2(\boldsymbol{v}_i \boldsymbol{v}_j) = -1/2$ with $\boldsymbol{v}_i \perp \boldsymbol{v}_j$.

For $I_{222}[D]$ the calculation is complicated by the fact that there are no explicit formulas for the real Gaunt coefficients. In order to calculate it a few more

passages are required:

$$
\begin{aligned}
I_{222}[D] = & \sum_{m_1 m_2 m_3} c_{2m_1} c_{2m_2} c_{2m_3} G(2, m_1 | 2, m_2 | 2, m_3) \\
= & \sum_{m_1 m_2 m_3} \left(\frac{8\pi}{15}\right)^3 \left[\sum_{i=1}^{3} \lambda_i Y_2^{m_1}(\boldsymbol{v}_i)\right] \left[\sum_{j=1}^{3} \lambda_j Y_2^{m_2}(\boldsymbol{v}_j)\right] \times \\
& \times \left[\sum_{k=1}^{3} \lambda_k Y_2^{m_3}(\boldsymbol{v}_k)\right] G(2, m_1 | 2, m_2 | 2, m_3) \\
= & \left(\frac{8\pi}{15}\right)^3 \sum_{m_1 m_2 m_3} \sum_{ijk} \lambda_i \lambda_j \lambda_k Y_2^{m_1}(\boldsymbol{v}_i) Y_2^{m_2}(\boldsymbol{v}_j) Y_2^{m_3}(\boldsymbol{v}_k) \times \\
& \times G(2, m_1 | 2, m_2 | 2, m_3) \\
= & \left(\frac{8\pi}{15}\right)^3 \sum_{m_1 m_2 m_3} \sum_{ijk} \lambda_i \lambda_j \lambda_k Y_2^{m_1}(\boldsymbol{v}_i) Y_2^{m_2}(\boldsymbol{v}_j) Y_2^{m_3}(\boldsymbol{v}_k) \times \\
& \times \int_{S^2} Y_2^{m_1}(\boldsymbol{u}) Y_2^{m_2}(\boldsymbol{u}) Y_2^{m_3}(\boldsymbol{u}) d\boldsymbol{u} \\
= & \left(\frac{8\pi}{15}\right)^3 \sum_{m_1 m_2 m_3} \sum_{ijk} \lambda_i \lambda_j \lambda_k \int_{S^2} Y_2^{m_1}(\boldsymbol{v}_i) Y_2^{m_1}(\boldsymbol{u}) Y_2^{m_2}(\boldsymbol{v}_j) Y_2^{m_2}(\boldsymbol{u}) \times \\
& \times Y_2^{m_3}(\boldsymbol{v}_k) Y_2^{m_3}(\boldsymbol{u}) d\boldsymbol{u} \\
= & \left(\frac{8\pi}{15}\right)^3 \sum_{ijk} \lambda_i \lambda_j \lambda_k \int_{S^2} \sum_{m_1=-2}^{2} Y_2^{m_1}(\boldsymbol{v}_i) Y_2^{m_1}(\boldsymbol{u}) \times \\
& \times \sum_{m_2=-2}^{2} Y_2^{m_2}(\boldsymbol{v}_j) Y_2^{m_2}(\boldsymbol{u}) \sum_{m_3=-2}^{2} Y_2^{m_3}(\boldsymbol{v}_k) Y_2^{m_3}(\boldsymbol{u}) d\boldsymbol{u} \\
= & \left(\frac{8\pi}{15}\right)^3 \sum_{ijk} \lambda_i \lambda_j \lambda_k \int_{S^2} \left(\frac{5}{4\pi}\right)^3 P_2(\boldsymbol{u} \cdot \boldsymbol{v}_i) P_2(\boldsymbol{u} \cdot \boldsymbol{v}_j) P_2(\boldsymbol{u} \cdot \boldsymbol{v}_k) d\boldsymbol{u} \\
= & \frac{8}{27} \sum_{i=1}^{3} \sum_{j=1}^{3} \sum_{k=1}^{3} \lambda_i \lambda_j \lambda_k \int_{S^2} P_2(\boldsymbol{u} \cdot \boldsymbol{v}_i) P_2(\boldsymbol{u} \cdot \boldsymbol{v}_j) P_2(\boldsymbol{u} \cdot \boldsymbol{v}_k) d\boldsymbol{u}
\end{aligned}
\tag{22}
$$

In order to solve the integral we need to consider the fact that $\boldsymbol{v}_1$, $\boldsymbol{v}_2$ *and* $\boldsymbol{v}_3$ *are three mutually orthogonal unit vectors. Considering* $\boldsymbol{x}$, $\boldsymbol{y}$, *and* $\boldsymbol{z}$ *the canonical Cartesian axes we can rename the eigenvectors as* $\boldsymbol{v}_1 = \boldsymbol{R}\boldsymbol{x}$, $\boldsymbol{v}_2 = \boldsymbol{R}\boldsymbol{y}$ *and* $\boldsymbol{v}_3 = \boldsymbol{R}\boldsymbol{z}$ *where* $\boldsymbol{R}$ *is a rotation matrix.*
Each of the dot products can be rewritten as $\boldsymbol{u} \cdot \boldsymbol{R}\boldsymbol{x}$, $\boldsymbol{u} \cdot \boldsymbol{R}\boldsymbol{y}$, *and* $\boldsymbol{u} \cdot \boldsymbol{R}\boldsymbol{z}$ *which are equivalent to* $\boldsymbol{u}^* \cdot \boldsymbol{x}$, $\boldsymbol{u}^* \cdot \boldsymbol{y}$, *and* $\boldsymbol{u}^* \cdot \boldsymbol{z}$ *with* $\boldsymbol{u}^* = \boldsymbol{R}^T \boldsymbol{u}$. *These operation are equivalent to the projection of* $\boldsymbol{u}^*$ *on the three Cartesian axes:*

$$
\begin{aligned}
u_1 &= \boldsymbol{u}^* \cdot \boldsymbol{x} = \sin(\theta)\cos(\phi) && (23) \\
u_2 &= \boldsymbol{u}^* \cdot \boldsymbol{y} = \sin(\theta)\sin(\phi) && (24) \\
u_3 &= \boldsymbol{u}^* \cdot \boldsymbol{z} = \cos(\theta) && (25)
\end{aligned}
$$

with θ *and* ϕ *the elevation and the azimuth of* $\boldsymbol{u}^*$. *Since the integral is all over*

S^2 *we can replace* $\boldsymbol{u}$ *with* $\boldsymbol{u}^*$ *obtaining*

$$\begin{aligned} I_{222}[D] &= \frac{8}{27}\sum_{i=1}^{3}\sum_{j=1}^{3}\sum_{k=1}^{3}\lambda_i\lambda_j\lambda_k\int_{S^2}P_2(u_i)P_2(u_j)P_2(u_k)d\boldsymbol{u} \\ &= \frac{8}{27}\sum_{i=1}^{3}\sum_{j=1}^{3}\sum_{k=1}^{3}\lambda_i\lambda_j\lambda_k\int_{\theta=0}^{\pi}\int_{\phi=0}^{2\pi}P_2(u_i)P_2(u_j)P_2(u_k)\sin(\theta)d\theta d\phi \\ &= \frac{8}{27}\sum_{i=1}^{3}\sum_{j=1}^{3}\sum_{k=1}^{3}\lambda_i\lambda_j\lambda_k\Upsilon(i,j,k) \end{aligned} \tag{26}$$

with $\Upsilon(i,j,k) = \frac{8\pi}{35}$ *if* $i=j=k$ *or* $i\neq j\neq k$. $\Upsilon(i,j,k) = -\frac{4\pi}{35}$ *if* $i\neq j=k$ *or* $i=j\neq k$ *or* $i=k\neq j$. *Substituting* Υ *we finally obtain:*

$$\begin{aligned} I_{222}[D] = \frac{32\pi}{945}\Big[&2\big(\lambda_1^3+\lambda_2^3+\lambda_3^3\big) - 3\big(\lambda_1^2\lambda_2+\lambda_1^2\lambda_3+\lambda_1\lambda_2^2+\lambda_1\lambda_3^2+ \\ &+\lambda_2^2\lambda_3+\lambda_2\lambda_3^2\big) + 12\lambda_1\lambda_2\lambda_3\Big]. \end{aligned} \tag{27}$$

5 Derivation of the microstructural kernel

The diffusion signal can be modeled as

$$E(b,\boldsymbol{u}) = \int_{S^2} E_{FRF}(b,\boldsymbol{u}|\boldsymbol{v})\rho(\boldsymbol{v})d\boldsymbol{v}. \tag{28}$$

where the single bundles of fiber response E_{FRF} *is modeled as*

$$E_{FRF}(b,\boldsymbol{u}|\boldsymbol{v}) = \sum_{i}^{C}\nu_i\exp\left(-b\left[(\lambda_{\parallel,i}-\lambda_{\perp,i})(\boldsymbol{u}^T\boldsymbol{v})^2+\lambda_{\perp,i}\right]\right) \tag{29}$$

and the fODF ρ *as*

$$\rho(\boldsymbol{v}) = \sum_{l=0,even}^{L}\sum_{m=-l}^{l}c_{lm}Y_l^m(\boldsymbol{v}). \tag{30}$$

Substituting Eq. (**??**) *and Eq.* (**??**) *into Eq.* (**??**) *we obtain*

$$\begin{aligned} E(b,\boldsymbol{u}) =& \int_{S^2}\sum_{i}^{C}\nu_i\exp\left(-b\left[(\lambda_{\parallel,i}-\lambda_{\perp,i})(\boldsymbol{u}^T\boldsymbol{v})^2+\lambda_{\perp,i}\right]\right)\times \\ &\times\sum_{l=0,even}^{L}\sum_{m=-l}^{l}c_{lm}Y_l^m(\boldsymbol{v})d\boldsymbol{v} \\ =&\sum_{i}^{C}\sum_{l=0,even}^{L}\sum_{m=-l}^{l}c_{lm}\nu_i\int_{S^2}\exp\left(-b\left[(\lambda_{\parallel,i}-\lambda_{\perp,i})(\boldsymbol{u}^T\boldsymbol{v})^2+\lambda_{\perp,i}\right]\right)\times \\ &\times Y_l^m(\boldsymbol{v})d\boldsymbol{v} \\ =&\sum_{i}^{C}\sum_{l=0,even}^{L}\sum_{m=-l}^{l}c_{lm}\nu_i\exp(-b\lambda_{\perp,i})\int_{S^2}\exp\left(-b(\lambda_{\parallel,i}-\lambda_{\perp,i})(\boldsymbol{u}^T\boldsymbol{v})^2\right)\times \\ &\times Y_l^m(\boldsymbol{v})d\boldsymbol{v}. \end{aligned} \tag{31}$$

We can apply the *Funk-Hecke Theorem* to the integral in Eq. (**??**) obtaining

$$
\begin{aligned}
E(b,\mathbf{u}) = & \sum_{l=0,even}^{L} \sum_{m=-l}^{l} c_{lm} Y_l^m(\mathbf{u}) \sum_{i}^{C} \nu_i \exp(-b\lambda_{\perp,i}) 2\pi \times \\
& \times \int_{-1}^{1} \exp\left(-b(\lambda_{\parallel,i} - \lambda_{\perp,i})t^2\right) P_l(t) dt \qquad (32) \\
= & \sum_{l=0,even}^{L} \sum_{m=-l}^{l} c_{lm} Y_l^m(\mathbf{u}) \sum_{i}^{C} \nu_i \exp(-b\lambda_{\perp,i}) 2\pi \Psi_l(b(\lambda_{\parallel,i} - \lambda_{\perp,i}))
\end{aligned}
$$

with

$$
\Psi_l(\xi) = (-\xi)^{\frac{l}{2}} \frac{\Gamma(\frac{l}{2} + \frac{1}{2})}{\Gamma(l + \frac{3}{2})} {}_1F_1\left(\frac{l}{2} + \frac{1}{2}, l + \frac{3}{2}, -\xi\right). \qquad (33)
$$

Therefore, we can write the microstructural kernel $K_l(b,\mathbf{p})$ as

$$
K_l(b,\mathbf{p}) = \sum_{i}^{C} \nu_i 2\pi \exp(-b\lambda_{\perp,i}) \Psi_l(b(\lambda_{\parallel,i} - \lambda_{\perp,i})) \qquad (34)
$$

with parameters vector $\mathbf{p} = [\nu_1, \lambda_{\parallel,1}, \lambda_{\perp,1}, \ldots, \nu_C, \lambda_{\parallel,C}, \lambda_{\perp,C}]$.

6 Kullback-Leibler divergence matrix

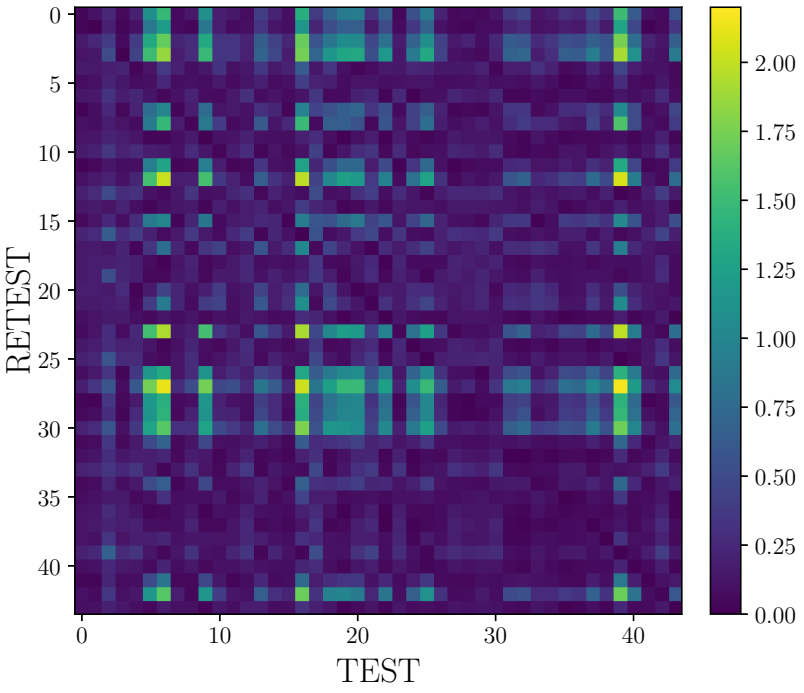

Figure 3: Kullback-Leibler divergence matrix for invariant $\hat{I}_{222}$ at b = 2000 mm^2/s between test and retest subjects.